Petroleum Science 20 (2023) 2165–2186

Contents lists available at ScienceDirect

Petroleum Science

journal homepage: www.keaipublishing.com/en/journals/petroleum-science

Original Paper

An unequal fracturing stage spacing optimization model for hydraulic fracturing that considers cementing interface integrity

Xu Han [a], Fu-Ping Feng [a, *], Xiao-Chuan Zhang [b], Jing Cao [c], Jun Zhang [a], Yu Suo [a], Yan Yan [c], Mao-Sen Yan [a]

[a] Department of Petroleum Engineering, Northeast Petroleum University, Daqing, 163318, Heilongjiang, China
[b] Daqing Oil Field Limited-Liability Company, Daqing, 163453, Heilongjiang, China
[c] Tubular Goods Research Institute of CNPC, Xi'an, 710000, Shaanxi, China

ARTICLE INFO

Article history:
Received 26 April 2022
Received in revised form
15 May 2023
Accepted 17 May 2023
Available online 18 May 2023

Edited by Yan-Hua Sun

Keywords:
Hydraulic fracturing
Cementing interface
Fracture propagation
Fracturing stage spacing
Wellbore integrity

ABSTRACT

Determining reasonable fracturing stage spacing is the key to horizontal well fracturing. Different from traditional stage spacing optimization methods based on the principle of maximum stimulated reservoir volume, in this paper, by considering the integrity of the wellbore interface, a fracture propagation model was established based on displacement discontinuity method and the competition mechanism of multifracture joint expansion, leading to the proposal of an unequal stage spacing optimization model. The results show that in the first stage, the interfacial fractures spread symmetrically along the axis of the central point during that stage, while in the second and subsequent stages, the interfacial fractures of each cluster extend asymmetrically along the left and right sides. There are two kinds of interface connectivity behaviour: in one, the existing fractures first extend and connect within the stage, and in the other, the fractures first extend in the direction close to the previous stage, with the specific behaviour depending on the combined effect of stress shadow and flow competition during hydraulic fracture expansion. The stage spacing is positively correlated with the number of fractures and Young's modulus of the cement and formation and is negatively correlated with the cluster spacing and horizontal principal stress difference. The sensitivity is the strongest when the Young's modulus of the cement sheath is 10–20 GPa, and the sensitivity of the horizontal principal stress difference is the weakest.

1. Introduction

Tight shale reservoirs are characterized by low porosity and low permeability, such that hydraulic fracturing technology has become an effective means to increase their production (Conrod et al., 2020; Jia, 2017; Sun et al., 2021). After years of practice, research has shown that it is important to maximize the volume of reservoir stimulated by long horizontal completion and segmenting stage spacing. As a part of the fracturing process, the design of stage spacing plays a key role in improving the stimulation effect. At present, the optimization of stage spacing is mainly based on two optimization principles: one is to adjust the deflection angle of hydraulic fractures (HFs) to obtain the maximum swept area of the fracture net (Li et al., 2017a; Luo et al., 2021; Xu et al., 2021; Yong et al., 2017; Zhang et al., 2021); the second is to avoid the expansion and mutual suppression of adjacent fractures under the action of stress interference (Al-Rbeawi, 2019; Taleghani, 2011; Wang, 2016; Xu et al., 2011; Michael, 2021). Although the optimized stage spacing has achieved a certain stimulation effect, nonetheless it also destroys the wellbore integrity. In addition to producing hydraulic fractures perpendicular to the wellbore, hydraulic fracturing leads to the debonding of cementing interfaces around the perforation and thus produces fractures along the interface. At this time, multiple HFs and interface fractures (IFs) typically expand together under the condition of fracturing fluid injection. The high-pressure fracturing fluid injected from the wellhead enters the cracks and overcomes the interfacial stress, causing further separation of the interface. As the fluid continues to be injected, the length of the hydraulic fracture and interfacial fracture expand together and continue to extend along their respective directions

* Corresponding author.
E-mail address: fupingfeng@126.com (F.-P. Feng).

https://doi.org/10.1016/j.petsci.2023.05.010

(Bois et al., 2012; Zhang and Bachu, 2011). As shown in Fig. 1, the influence on well integrity of the interface failure zone formed during synchronous propagation of HFs and IFs is always ignored. Existing research has shown that 11–18 m and 5–8 m axial fractures will occur at the casing–cement interface (CCI) and cement–formation interface (CFI), respectively, during single-cluster hydraulic fracture propagation (Jiang et al., 2020; Xu et al., 2021; Zhu et al., 2013). In recent years, the multifracturing horizontal well with tighter clusters has become a core technology that is now widely used in North America to increase production and efficiency (Jacobs, 2019). It also represents a new breakthrough in the study and application of shale reservoir reconstruction technology in China. This technology not only increases the number of clusters in a single stage but also shortens the cluster spacing to less than 10 m, effectively improving resource production (Xu et al., 2018a). However, some of the wells tested showed that even though the cementing quality was good, sealing failure occurred after subsequent stimulation, for example by additional fracturing. This means that a cluster spacing that is too small is more likely to cause interfacial fracture propagation and connect the whole horizontal section, resulting in serious consequences such as fracturing fluid leakage, channelling between stages, causing damage, and reduced well life.

At present, scholars are more concerned about the expansion of HFs and IFs during hydraulic fracturing, with only a few focused on the integrity of the wellbore seal. Lecampion et al. (2011) combined experiments with numerical simulations to investigate the axial propagation length and circumferential propagation of the cementing interface crack, with results showing that the IFs tended to a constant value in the circumferential direction with fluid injection and expanded along the axial direction of the wellbore. Wang et al. (2021) simulated the changes in cementing interface stress and fracture width during fracturing by characterizing the stress intensity factor of the CFI but did not clarify the axial propagation law of IFs. Li et al. (2017b) and Feng et al. (2017) studied the axial expansion length and circumferential expansion direction of the annulus at the cementing interface based on experiments, mathematical models, and numerical simulations. Nevertheless, in the above studies, fracturing fluid was directly injected into IFs, which cannot reflect the flow distribution of multiple fractures during an actual fracturing event, meaning that the calculated IF length would be much higher than the real value. In this paper, the displacement discontinuity method (DDM) was combined with the fluid flow equation to study the fracture flow rate distribution under fluid–structure coupling conditions. Considering the coupling effect between pore fluid and rock deformation, Wang and Taleghani (2017) used the finite element method (FEM) to simulate the initiation and propagation process of IFs during fracturing and analysed the potential failure possibility of the interface. A large number of studies have shown that HFs present different geometric forms under different fracturing conditions. This means that the IFs also change. In this paper, the results of the above study are continued to further quantify the axial propagation length of the IFs.

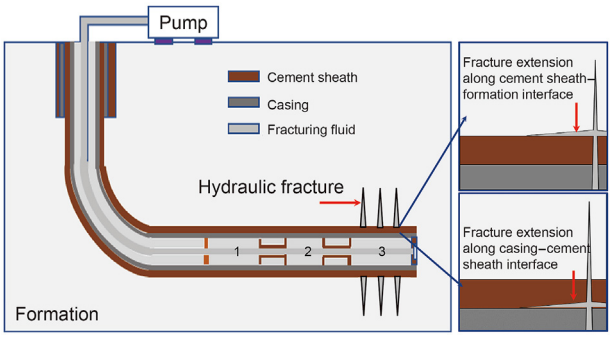

Fig. 1. Propagation of interface fractures during hydraulic fracturing.

At present, there are many numerical methods to study the fracture of the cementing interface. Tan et al. (2018) discussed the influence of the cementation strength of bedding planes on HF propagation based on the discrete element method (DEM). Zhong et al. (2014), Xu et al. (2018b), and Chen et al. (2009) used the finite element method (FEM) to calculate fracture propagation at the CFI; Li et al. (2020) and Sheikhmali (2016) used the extended finite element method (XFEM) to describe the propagation behaviour of mixed mode fractures. The above methods have unique advantages in the study of hydraulic fracturing, in which the stress singularity of the fracture tip cannot be avoided. Gu and Zhang (2020) successfully solved the fracture mechanics parameters of bimaterial IFs by introducing the boundary element regularization algorithm. The results showed that this method significantly reduced the stress oscillation near the fracture tip. As an indirect boundary element method (BEM), the displacement discontinuity method (DDM) has the characteristics of node discretization and is also widely used in fluid structure coupling. Thus, DDM is also the method chosen in this paper. Moreover, by introducing the fracture toughness of two-material interface fracture propagation, the calculation conditions are more consistent with the actual conditions.

In this paper, two models are established based on the fluid–structure interaction theory, one is the synchronous propagation model of planar 2D hydraulic fractures based on displacement discontinuity theory, the other is the propagation model of nonplanar 3D cementing interface fractures, and the equivalent propagation lengths of the IFs in the stages are obtained by simulating the fracture geometry, net pressure, and flow rate distribution. Finally, an unequal stage spacing optimization model is proposed based on the principle of maintaining the integrity of the wellbore. The results can provide a theoretical basis for the optimal design of fracturing parameters.

2. Methods and models

After the completion of a horizontal well, perforation is carried out in turn, and fracturing fluid is pumped in. The initial damage around the cementing interface is caused by the perforation and expands axially under the action of the high-pressure fluid. All clusters of fractures in the stage crack simultaneously, which affects the wellbore integrity. According to the above process, the following assumptions are made for the model:

(1) The tip propagation of the HF and IF meets the linear fracture mechanics;
(2) There are no natural fractures in the reservoir;
(3) The fracturing fluid is an incompressible Newtonian fluid that fills the fractures;
(4) The cement sheath and formation are linear elastomers;
(5) Each perforation cluster produces only one fracture;
(6) The hydraulic fracture accords with the hypothesis of the KGD model, in which the planar 3D fracture has a fixed fracture height.

2.1. Judgement of the IF propagation position

It is generally believed that the stress on the cementing interface during hydraulic fracturing arises from two factors: one is the fluid

pressure in the wellbore (Adams et al., 2017), and the other is the nonuniform *in-situ* stress (Deng et al., 2021; Huan et al., 2021). Yan et al. (2020) noted that the degree of compaction of the CFI is greater under the formation confining pressure and that the fracturing fluid more easily enters the CCI. Wang et al. (2021) showed that when fractures exist at both cementing interfaces, the fractures at the CFI are wider than those at the CCI. The difference in the above conclusions is caused by different initial conditions. In fact, in the case of non-creep formation, the *in-situ* stress around the borehole is redistributed and stable after the rock is removed from the borehole. After the cement slurry enters the hole and solidifies, the formation has no initial force on the cement sheath (Shi et al., 2015; Saint-Marc et al., 2008; Fan et al., 2019). Therefore, the equilibrium state of casing–cement–formation before fracturing fluid injection is regarded as the initial state, and the IF propagation conditions should meet the following principles:

$$\begin{cases} p_{f1} \geq \sigma_{cc} + \sigma_{t1} \\ p_{f2} \geq \sigma_{cf} + \sigma_{t2} \end{cases} \tag{1}$$

where p_{f1} and p_{f2} are the fracture injection pressures at CCI and CFI, Pa; σ_{cc} and σ_{cf} are the radial stresses of CCI and CFI, Pa; and σ_{t1} and σ_{t2} are the bonding strengths of CCI and CFI, Pa.

According to the theory of thick-walled cylinders, the radial stress on the interfaces during fracturing can be expressed by the following formula (Chu et al., 2015):

$$\begin{cases} \sigma_{cc} = \dfrac{f_1(f_6+f_7)p_{in} + f_4 f_8 \sigma_{ou}}{f_4 f_5 - (f_3 - f_2)(f_6+f_7)} \\ \sigma_{cf} = \dfrac{f_2 f_5 p_{in} + f_8(f_2+f_3)\sigma_{ou}}{f_4 f_5 - (f_3+f_2)(f_6-f_7)} \end{cases} \tag{2}$$

where p_{in} is the fluid pressure in the wellbore, Pa; σ_{ou} is the *in-situ* stress of the far field, Pa; and f_1–f_8 are the functional expressions of the radius, Young's modulus, and Poisson's ratio of the casing, cement sheath, and formation, respectively (see Appendix A for details).

2.2. Fracture propagation model under fluid–solid coupling

2.2.1. Rock deformation equation under staged fracturing

Assuming that all clusters of fractures in each stage expand simultaneously, when fracturing Fracture 1 in Stage 1, the fracture is divided into N_1 discontinuous displacement units, and the stress and displacement distribution of element i between fractures can be calculated by the following formula (Wu and Olson, 2015):

$$\begin{cases} \sigma_n^i = \sum_{j=1}^{N_1} G^{ij} C_{ns}^{ij} D_s^j + \sum_{j=1}^{N_1} G^{ij} C_{nn}^{ij} D_n^j \\ \sigma_s^i = \sum_{j=1}^{N_1} G^{ij} C_{ss}^{ij} D_s^j + \sum_{j=1}^{N_1} G^{ij} C_{sn}^{ij} D_n^j \end{cases} \tag{3}$$

where σ_n is the normal stress, Pa; σ_s is the tangential stress, Pa; D_n is the normal displacement discontinuity, m; D_s is the tangential displacement discontinuity, m; C_{ns}^{ij}, C_{nn}^{ij}, C_{ss}^{ij}, and C_{sn}^{ij} are the elastic coefficient matrices composed of elements i and j in the calculation domain; G_{ij} is the seam height correction factor (Olson, 2004):

$$G^{ij} = 1 - \frac{d_{ij}^{\beta}}{\left[d_{ij}^2 + (h/\alpha)^2\right]^{\beta/2}} \tag{4}$$

where d_{ij} is the distance between cells, m; h is the fracture height, m; and α and β are empirical parameters (Li et al., 2020), taken as $\alpha = 1$, $\beta = 2.3$.

When fracturing n fractures in Section 1, Eq. (3) can be rewritten as:

$$\begin{cases} \sigma_n^i = \sum_{j=1}^{N_1+N_2+\ldots+N_n} G^{ij} C_{ns}^{ij} D_s^j + \sum_{j=1}^{N_1+N_2+\ldots+N_n} G^{ij} C_{nn}^{ij} D_n^j \\ \sigma_s^i = \sum_{j=1}^{N_1+N_2+\ldots+N_n} G^{ij} C_{ss}^{ij} D_s^j + \sum_{j=1}^{N_1+N_2+\ldots+N_n} G^{ij} C_{sn}^{ij} D_n^j \end{cases} \tag{5}$$

Let $M_1 = N_1 + N_2 + \ldots + N_n$ represent the total number of units divided by each fracture in Stage 1; then, the displacement discontinuity caused by each fracture in the M-th stage ($M > 1$) can be expressed by the following formula:

$$\begin{cases} \sigma_n^i = \sum_{j=1}^{M_1+M_2+\ldots+M_m} G^{ij} C_{ns}^{ij} D_s^j + \sum_{j=1}^{M_1+M_2+\ldots+M_m} G^{ij} C_{nn}^{ij} D_n^j \\ \sigma_s^i = \sum_{j=1}^{M_1+M_2+\ldots+M_m} G^{ij} C_{ss}^{ij} D_s^j + \sum_{j=1}^{M_1+M_2+\ldots+M_m} G^{ij} C_{sn}^{ij} D_n^j \end{cases} \tag{6}$$

2.2.2. Fluid flow equation

The Navier–Stokes equation is used to represent the flow of fluid in rock fractures (Wu, 2014). Assuming that the Newtonian fluid flows in two smooth plates without relative slip, the Navier–Stokes equation can be simplified as follows:

$$\frac{\partial p}{\partial x} = 2^{n'+1} k' \left(\frac{1+2n'}{n'}\right)^{n'} \frac{1}{w^{2n'+1}} \frac{q}{H}\left|\frac{q}{H}\right|^{n'-1} \tag{7}$$

where p is the fluid pressure, Pa; q is the fluid flow rate, m^2/s; H is the height of the fracture, m; w is the width of the fracture, m; x is the distance along the fracture, m; n' is the fluid power-law index; and k' is the consistency coefficient, $Pa \cdot s^n$.

Cheng (2016) compared the fracture propagation results with and without fluid leakage terms based on the KGD model, finding that the fracture length expanded faster when not considering fluid loss. However, the presence of the fluid leakage term only affects the propagation speed of the fracture. With a sufficiently long fluid injection time, the final propagation length of the fracture is similar. Since staged fracturing is mostly used in low permeability reservoirs and the hydraulic fracture propagation model in this paper is also based on the assumptions of the KGD model, the fluid filtration process is ignored in the fracturing process presented here (Hou et al., 2015; Kumar and Ghassemi, 2016; Chen et al., 2019), and the material balance equation meets the following requirements:

$$\frac{\partial q(x,t)}{\partial x} - \frac{\partial A(x,t)}{\partial t} = 0 \tag{8}$$

where $q(x,t)$ is the volume flow of liquid in the fracture at time t, m^3/s; and $A(x,t)$ is the cross-sectional area of the fracture at time t, m^2.

Wu (2014) deduced the continuity equation of multiple fracture pressures. The wellbore internal pressure is the sum of the fracture inlet pressure, perforation friction pressure drops, and wellbore friction pressure drop, given in the following formula as:

$$p_{in} = p_{w,i} + p_{pf,i} + p_{cf,i} \tag{9}$$

$$\frac{\partial p_w}{\partial s}=2^{n'+1}k'\left(\frac{1+2n'}{n'}\right)^{n'}h^{-n'}w^{-(2n'+1)}Q_i^{n'} \tag{10}$$

$$p_{\mathrm{pf},i}=\frac{0.2369\rho_s}{n_{p,i}^2d_{p,i}^4K_d^2}Q_i^2 \tag{11}$$

$$p_{\mathrm{cf},i}=2^{3n'+2}\pi^{-n'}k'\left(\frac{1+3n'}{n'}\right)^{n'}D^{-(3n'+1)}\sum_{j=1}^{i}(s_j-s_{j-1})Q_{w,j}{}^{n'} \tag{12}$$

where p_{in} is the total pressure at the wellbore heel, Pa; $p_{w,i}$ is the pressure at the fracture entrance, Pa; $p_{\mathrm{pf},i}$ is the perforation friction pressure loss, Pa; $p_{\mathrm{cf},i}$ is the pressure loss in the horizontal wellbore, Pa; w is the fracture width, m; Q_i is the flow rate in crack i , m^3/s; $\rho_{\mathbf{s}}$ is the density of the slurry, kg/m^3; $n_{\mathrm{p},i}$ is the number of perforations of HF; $d_{\mathrm{p},i}$ is the diameter of perforation of HF, m; and D is the diameter of the wellbore, m.

2.2.3. Fluid volume conservation in fractures

The pump rate is the sum of the rate of each HF and IF, that is:

$$Q_{\mathrm{T}}=\sum_{i=1}^{N}Q_i+\sum_{j=1}^{M}Q_j \tag{13}$$

where Q_{T} is the total injection rate, m^3/s; Q_j is the rate of IF j, m^3/s.

Different from the conventional bimaterial plate IF, in this paper, a cylindrical IF is considered, which spans an arc of angle 2ϑ of a cylinder with radius r. It is assumed that the axial propagation length of the fracture is much larger than its arc length ($l>2\vartheta r$), taking the CCI as an example (see Fig. 2) (Lecampion et al., 2013). In this case, the cylinder with IF can be decomposed into plane strains of multiple horizontal sections (Farris et al., 1989).

The Lamé solution shows a numerical method for solving the interfacial crack of two materials (Toya, 1974; Piva, 1982; Lecampion et al., 2013) with a circular tube in the case of local orientation debonding ($\vartheta>\pi$). The functional relationship between the radial opening of the IF and the pressure in the fracture is established using the continuity criterion of radial displacement at the interface:

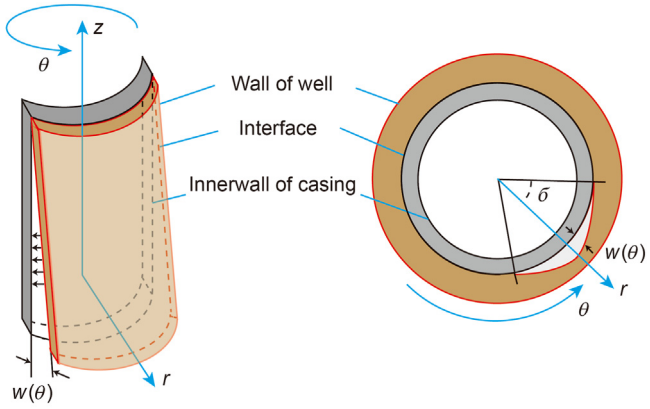

Fig. 2. Diagram of the IF cross section.

$$w(\theta)=\left[u_r^j-u_r^{j+1}\right]_{r=R_j}=2\vartheta R_j\frac{p}{\chi},\quad \theta\in[-\vartheta,\vartheta] \tag{14}$$

where p is the net pressure in the fracture, Pa; χ is a function of the wellbore radius, Young's modulus, and Poisson's ratio.

The CCI is expressed as follows:

$$\frac{1}{\chi}=\frac{r_1^2+r_2^2(1-2\nu_1)}{2G_1(r_2^2-r_1^2)}+\frac{r_2^2(G_2-G_3)(1-2\nu_2)+r_3^2(G_2+G_3(1-2\nu_2))}{2G_2\left[r_2^2(G_3-G_2)+r_3^2(G_2+G_3(1-2\nu_2))\right]}$$

The CFI is expressed as follows:

$$\frac{1}{\chi}=\frac{2}{G_3}+\frac{1}{G_2}\frac{r_3^2\left[r_1^2(G_1-G_2)-r_2^2\alpha_1\right](1-2\nu_2)-r_2^2\left[r_1^2\alpha_1-r_2^2\kappa\right]}{2r_1^2\left[r_3^2(G_1-G_2)+r_2^2\alpha_2\right]-2r_2^2(r_3^2\alpha_1+r_2^2\kappa)}$$

$$G=E/2(1+\nu)$$
$$\alpha_1=G_1+G_2(1-2\nu_1)$$
$$\alpha_2=G_2+G_1(1-2\nu_2)$$
$$\kappa=G_1(1-2\nu_2)-G_2(1-2\nu_1)$$

where subscripts 1, 2, and 3 represent the casing, cement sheath, and formation, respectively. E is Young's modulus, Pa; and ν is Poisson's ratio.

Before fracture connection in the section, according to volume conservation, the total volume of fluid pumped during the fracturing time is equal to the fluid volume in the HF and IF:

$$\int_0^t Q_{\mathrm{T}}(t)\mathrm{d}t=\sum_{i=1}^{N}\int_0^{L_i(t)}hw_{\mathrm{HF}}\mathrm{d}s+\sum_{j=1}^{M}\int_0^t Q_j\mathrm{d}t \tag{15}$$

$$Q_j=\int_{-\vartheta}^{\vartheta}\int_{-w(\theta)/2}^{w(\theta)/2}v_jr_j\mathrm{d}r\mathrm{d}\theta \tag{16}$$

where $L_i(t)$ is the total fracture length of HF i at time t, m; v is the fluid velocity profile, m/s, which can be calculated according to Poiseuille's law (Batchelor, 1967):

$$v(\theta,r)=\frac{1}{2\mu_{\mathrm{f}}}\left[r^2-\frac{w(\theta)^2}{4}\right]\frac{\partial p}{\partial x} \tag{17}$$

where μ_{f} is the fluid viscosity, Pa·s.

After fracture connection in the stage, the length of the fracture is equal to the length of the stage, and the HFs on both sides of the stage and the IFs between them can be regarded as a domain. Assuming that the IFs are regarded as having equal width, the total fluid volume is the sum of the flow in the domain and the IF volume on both sides of the domain. It can be regarded as a single HF, and the IFs on both sides expand together. Then, Eq. (13) can be rewritten as follows:

$$\int_0^t Q_{\mathrm{T}}(t)\mathrm{d}t=\int_0^{L(t)}hw_{\mathrm{HF}}\mathrm{d}s+\sum_{j=1}^{2}\int_0^t Q_j\mathrm{d}t+l(\theta)w(\theta)L_{\mathrm{fs}} \tag{18}$$

where $l(\theta)$ is the arc length corresponding to the circumferential extension angle θ, m; L_{fs} is the length of the total stage, m.

2.2.4. Fracture propagation criterion

2.2.4.1. Propagation of HFs. According to linear fracture mechanics, the expression of the stress field at any point near the tip of a mixed type I and II fracture is as follows (Cong et al., 2022):

$$\begin{Bmatrix}\boldsymbol{\sigma}_{xx}\\ \boldsymbol{\sigma}_{yy}\\ \boldsymbol{\sigma}_{xy}\end{Bmatrix}=\frac{K_{\mathrm{I}}}{\sqrt{2\pi r}}\begin{Bmatrix}\cos\frac{\theta}{2}\left(1-\sin\frac{\theta}{2}\sin\frac{3\theta}{2}\right)\\ \cos\frac{\theta}{2}\left(1+\sin\frac{\theta}{2}\sin\frac{3\theta}{2}\right)\\ \cos\frac{\theta}{2}\sin\frac{\theta}{2}\sin\frac{3\theta}{2}\end{Bmatrix}+\frac{K_{\mathrm{II}}}{\sqrt{2\pi r}}\begin{Bmatrix}\sin\frac{\theta}{2}\left(-2-\cos\frac{\theta}{2}\cos\frac{3\theta}{2}\right)\\ \sin\frac{\theta}{2}\cos\frac{\theta}{2}\cos\frac{3\theta}{2}\\ \cos\frac{\theta}{2}\left(1-\sin\frac{\theta}{2}\sin\frac{3\theta}{2}\right)\end{Bmatrix} \tag{19}$$

where K_{I} and K_{II} are the type I and type II stress intensity factors, respectively, Pa·m$^{1/2}$; $\boldsymbol{\sigma}_{xx}$, $\boldsymbol{\sigma}_{yy}$, and $\boldsymbol{\sigma}_{zz}$ are the stress components of the rock mass around HF in the rectangular coordinate system, Pa. After coordinate transformation, the stress component near the fracture tip in polar coordinates can be expressed as:

$$\sigma_r=\frac{1}{\sqrt{2\pi r}}\cos\frac{\theta}{2}\left[K_{\mathrm{I}}\left(1+\sin^2\frac{\theta}{2}\right)+\frac{3}{2}K_{\mathrm{II}}\sin\theta-2K_{\mathrm{II}}\tan\theta\right]$$

$$\sigma_\theta=\frac{1}{\sqrt{2\pi r}}\cos\frac{\theta}{2}\left[K_{\mathrm{I}}\cos\frac{\theta}{2}-\frac{3}{2}K_{\mathrm{II}}\sin\theta\right]$$

$$\tau_{r\theta}=\frac{1}{\sqrt{2\pi r}}\cos\frac{\theta}{2}\left[K_{\mathrm{I}}\sin\theta+K_{\mathrm{II}}(3\cos\theta-1)\right]$$

The maximum circumferential stress criterion states that the fracture propagates along the direction of the maximum circumferential stress. The continuous function is adopted to obtain the maximum value, and the direction θ corresponding to $\sigma_{\theta\max}$ satisfies:

$$\frac{\partial\sigma_\theta}{\partial\theta}=0,\quad \frac{\partial^2\sigma_\theta}{\partial\theta^2}<0$$

Wu (2014) derived the expression of the I-II composite fracture propagation direction when the fracture expands along the direction of maximum tensile stress:

$$\theta_0=\begin{cases}2\arctan\left(\frac{1}{4}\frac{K_{\mathrm{I}}}{K_{\mathrm{II}}}\pm\frac{1}{4}\sqrt{\left(\frac{K_{\mathrm{I}}}{K_{\mathrm{II}}}\right)^2+8}\right), & K_{\mathrm{II}}\neq0\\ 0^\circ, & K_{\mathrm{II}}=0\end{cases} \tag{20}$$

By transforming Eq. (18) into a polar coordinate system and further derivation, the I-II composite crack can be transformed into a pure type-I crack, and the equivalent stress intensity factor K_{e} is used to represent the composite stress intensity factor composed of K_{I} and K_{II} (Kim and Paulino, 2007):

$$K_{\mathrm{e}}=\frac{1}{2}\cos\frac{\theta_0}{2}\left[K_{\mathrm{I}}(1+\cos\theta_0)-3K_{\mathrm{II}}\sin\theta_0\right] \tag{21}$$

When $K_{\mathrm{e}}>K_{\mathrm{IC}}$, the HF expands.

Olson and his co-workers calculated the shear and normal displacement discontinuity functions at the fracture tip according to the DDM (Olson and Pollard, 1989; Olson, 2007), which can be expressed as follows:

$$\begin{aligned}K_{\mathrm{I}}&=\frac{0.806E\sqrt{\pi}}{4\left(1-\nu^2\right)\sqrt{2a}}D_{\mathrm{n}}\\ K_{\mathrm{II}}&=\frac{0.806E\sqrt{\pi}}{4\left(1-\nu^2\right)\sqrt{2a}}D_{\mathrm{s}}\end{aligned} \tag{22}$$

The stress of the fracture in Stage 1 is assumed to be the initial *in-situ* stress field $\boldsymbol{\Omega}_0$; then, the stress field of the fracture in Stage 2 is the superposition of the initial *in-situ* stress field and the stress field after fracturing in Stage 1:

$$\boldsymbol{\Omega}_1=\begin{bmatrix}\sigma_{xx}&\sigma_{xy}\\ \sigma_{yx}&\sigma_{yy}\end{bmatrix}_1+\boldsymbol{\Omega}_0 \tag{23}$$

When fracturing Section m, the initial stress field of HF propagation is the superposition of the stress field formed after fracturing in the above Section $m-1$:

$$\boldsymbol{\Omega}_m=\boldsymbol{\Omega}_0+\begin{bmatrix}\sigma_{xx}&\sigma_{xy}\\ \sigma_{yx}&\sigma_{yy}\end{bmatrix}_1+\begin{bmatrix}\sigma_{xx}&\sigma_{xy}\\ \sigma_{yx}&\sigma_{yy}\end{bmatrix}_2+\cdots+\begin{bmatrix}\sigma_{xx}&\sigma_{xy}\\ \sigma_{yx}&\sigma_{yy}\end{bmatrix}_{m-1} \tag{24}$$

2.2.4.2. Propagation of IFs. The fracture mode of an IF is different from that of a single material, and oscillatory singularities are often present. Rice (1988) proposed the relationship between the stress field and displacement field near the IF tip and the complex stress intensity factor based on the linear elastic hypothesis (Xu et al., 2000):

$$\left(\sigma_{\mathrm{in},y}+i\tau_{\mathrm{in},xy}\right)_{\vartheta=0}=\frac{K^*}{\sqrt{2\pi}}r^{*-1/2+i\varepsilon} \tag{25}$$

$$\begin{aligned}&\left(u_{\mathrm{in},y}+iu_{\mathrm{in},x}\right)_{\vartheta=\pi}-\left(u_{\mathrm{in},y}+iu_{\mathrm{in},x}\right)_{\vartheta=-\pi}\\ &=\frac{8}{(1+2i\varepsilon)\cosh(\pi\varepsilon)}\cdot\frac{K^*}{E_{\mathrm{in}}}\cdot\left(\frac{r^*}{2\pi}\right)^{1/2}\cdot r^{*i\varepsilon}\end{aligned} \tag{26}$$

where ε is the interface oscillation factor; K^* is the interface complex stress intensity factor, Pa·m$^{1/2}$; and E_{in} is the equivalent Young's modulus of the interface, Pa.

Based on the calculation method of the interface stress intensity factor proposed by Nagashima et al. (2003), combined with Eqs. (23) and (24), the displacement discontinuity form of the stress intensity factor at the IF tip can be obtained:

$$\begin{aligned}K_{\mathrm{I}}^*&=\frac{\delta_{\mathrm{n}}[\sin(\varepsilon\ln r^*)-2\varepsilon\cos(\varepsilon\ln r^*)]+\delta_{\mathrm{s}}[\cos(\varepsilon\ln r^*)+2\varepsilon\sin(\varepsilon\ln r^*)]}{\left(1+4\varepsilon^2\right)\xi}\\ K_{\mathrm{II}}^*&=\frac{\delta_{\mathrm{s}}[\cos(\varepsilon\ln r^*)+2\varepsilon\sin(\varepsilon\ln r^*)]-\delta_{\mathrm{n}}[\sin(\varepsilon\ln r^*)+2\varepsilon\cos(\varepsilon\ln r^*)]}{\left(1+4\varepsilon^2\right)\xi}\\ \xi&=\frac{8r^{*1/2}}{E_{\mathrm{in}}\left(1+4\varepsilon^2\right)(2\pi)^{1/2}\cosh(\pi\varepsilon)}\end{aligned} \tag{27}$$

where K_{I}^* and K_{II}^* are the stress intensity factors of type I and type II, Pa·m$^{1/2}$; δ_{n} is the normal displacement discontinuity of the IF, m; δ_{s} is the shear displacement discontinuity of the IF, m.

Yuuki et al. (1993, 1994) proposed that the stress intensity factor

presents an elliptical distribution during IF propagation, which can be described as:

$$K^*_{\mathrm{I,II}} = \left(\frac{K^P_{\mathrm{I}} - K^c_{\mathrm{I}}}{K^*_{\mathrm{IC}}}\right)^2 + \left(\frac{K^P_{\mathrm{II}} - K^c_{\mathrm{II}}}{K^*_{\mathrm{IIC}}}\right)^2 = 1 \tag{28}$$

where K^*_{IC} and K^*_{IIC} are the type-I and type-II fracture toughnesses of the interface; K^P_{I} and K^P_{II} are the type-I and type-II stress intensity factors under stress P; and K^c_{I} and K^c_{II} are the type-I and type-II stress intensity factors under the cohesion force (including normal stress and shear stress).

Since type I cracks are mainly subject to normal stress and type II cracks are mainly subject to shear stress, the above formula can be rewritten as:

$$\left(\frac{K^P_{\mathrm{I}} - K^\sigma_{\mathrm{I}}}{K^*_{\mathrm{IC}}}\right)^2 + \left(\frac{K^P_{\mathrm{II}} - K^\tau_{\mathrm{II}}}{K^*_{\mathrm{IIC}}}\right)^2 = 1 \tag{29}$$

where K^σ_{I} and K^τ_{II} are the type-I stress intensity factors under the action of normal stress in interfacial cohesion, and K^τ_{II} is the type-II stress intensity factor under the action of shear stress in interfacial cohesion.

K^*_{IC} indicates the ability of the interface to resist debonding, and K^*_{IIC} indicates the ability of the interface to resist shear force. When the interface stress intensity factor falls out of the ellipse, the IF expands along the interface.

2.3. Stage spacing of the fracturing section

Gu (1987) established the corresponding relationship between the stress intensity factor and propagation length when multiple fractures propagate together:

$$\Delta L_i(t) = \begin{cases} \dfrac{K^i_{\mathrm{e}}(t) - K_{\mathrm{IC}}}{K^i_{\mathrm{emax}}(t) - K_{\mathrm{IC}}} \cdot \Delta L_i(t - \Delta t), \ K^i_{\mathrm{e}}(t) > K_{\mathrm{IC}} \\ 0, \ K^i_{\mathrm{e}}(t) < K_{\mathrm{IC}} \end{cases}$$
$$\Delta l_j(t) = \begin{cases} \dfrac{K^{*j}(t) - K^*_{\mathrm{IC}}}{K^{*j}_{\mathrm{max}}(t) - K^*_{\mathrm{IC}}} \cdot \Delta l_j(t - \Delta t), \ K^{*j}(t) > K^*_{\mathrm{IC}} \\ 0, \ K^{*j}(t) < K^*_{\mathrm{IC}} \end{cases} \tag{30}$$

where $K^i_{\mathrm{emax}}(t)$ is the maximum stress intensity factor at the HF tip at time t; $K^i_{\mathrm{e}}(t)$ is the stress intensity factor at the HF tip at time t; $K^{*j}_{\mathrm{max}}(t)$ is the maximum stress intensity factor at the IF tip at time t; $K^{*j}(t)$ is the stress intensity factor at the IF tip at time t; $\Delta L_i(t)$ and $\Delta L_j(t)$ are the HF and IF propagation steps at time t; and Δt is the time step.

The reasonable spacing should be less than the connectivity distance of IFs between the stages, that is, the sum length of the IF, l_2, on the left of Stage 1 and the length of the IF, l_3, on the right of Stage 2. The spacing between the second stage and the first stage should be set as U_1, and so on, such that the spacing U_m between Stage $m+1$ and Stage m can be obtained as follows:

$$U_m = l_{2m} + l_{2m+1} \tag{31}$$

2.4. Model solution

For the coupling problem of rock deformation and fluid flow, the linear equations composed of rock deformation equations and the nonlinear equations composed of fluid flow equations should be solved simultaneously. The Newton–Raphson iterative method is adopted in this paper, which is also the most common method for solving nonlinear equations. This method has a fast convergence rate, and the solution of the equations can be obtained by iterating more than ten steps.

Fractures are subject to the joint action of far-field stress and fluid pressure, such that the corresponding vector-valued function is constructed according to the element stress balance equation as follows:

$$f_{\mathrm{I}} = \sigma^i_{\mathrm{n}} - \sum_{j=1}^{N} G^{ij} C^{ij}_{\mathrm{ss}} D^j_{\mathrm{s}} - \sum_{j=1}^{N} G^{ij} C^{ij}_{\mathrm{sn}} D^j_{\mathrm{n}}$$
$$f_{\mathrm{II}} = \sigma^i_{\mathrm{s}} - \sum_{j=1}^{N} G^{ij} C^{ij}_{\mathrm{ns}} D^j_{\mathrm{s}} - \sum_{j=1}^{N} G^{ij} C^{ij}_{\mathrm{nn}} D^j_{\mathrm{n}} \tag{32}$$

The corresponding vector-valued function is constructed as follows according to the pressure drop equilibrium equation:

$$f_{\mathrm{III}} = \frac{\partial p}{\partial x} - 2^{n'+1} k' \left(\frac{1 + 2n'}{n'}\right)^{n'} \frac{q^{n'}}{w_i^{2n'+1}} \tag{33}$$

The corresponding vector-valued function is constructed as follows according to the material balance equation for an incompressible fluid:

$$f_{\mathrm{IV}} = \frac{\partial q(x,t)}{\partial x} - \frac{\partial A(x,t)}{\partial t} \tag{34}$$

The wellbore fluid flow model is introduced in multifracture propagation, and the vector-valued function is constructed as follows:

$$f_{\mathrm{V}} = p_0 - \left(p_{w,j} + p_{\mathrm{pf},j} + p_{\mathrm{cf},j}\right) \tag{35}$$

The vector-valued function matrix and its corresponding solution vector can be formed by Eqs. (32)–(35):

$$[\boldsymbol{F}] = [f_{\mathrm{I}}, f_{\mathrm{II}}, f_{\mathrm{III}}, f_{\mathrm{IV}}, f_{\mathrm{V}}]^{\mathrm{T}} \tag{36}$$

$$[\boldsymbol{x}] = [D_{\mathrm{s}}, D_{\mathrm{n}}, p_i, \mathrm{d}t, p_0]^{\mathrm{T}} \tag{37}$$

According to the rock deformation equation, the stress in the tangent and normal directions of the fracture surface meets the following boundary conditions:

$$\begin{cases} \sigma_{\mathrm{n}} = p - \sigma^{\mathrm{n}}_{\mathrm{c}} \\ \sigma_{\mathrm{s}} = -\sigma^{\mathrm{s}}_{\mathrm{c}} \end{cases} \tag{38}$$

For the fluid flow equation, the fluid velocity at the fracture inlet should be the rate at which the wellbore enters the fracture, and the fluid velocity at the fracture tip is zero, that is:

$$q(0,t) = Q_{\mathrm{c}}, \ \ q\left(L_{\mathrm{f}}, t\right) = 0 \tag{39}$$

The displacement discontinuity of the fracture element can be obtained by the stress field, and then the stress intensity factors at the HF and IF tips are obtained to judge whether the fracture expands and to determine the direction of expansion. By iterating the process, the stress field and fracture propagation shape after

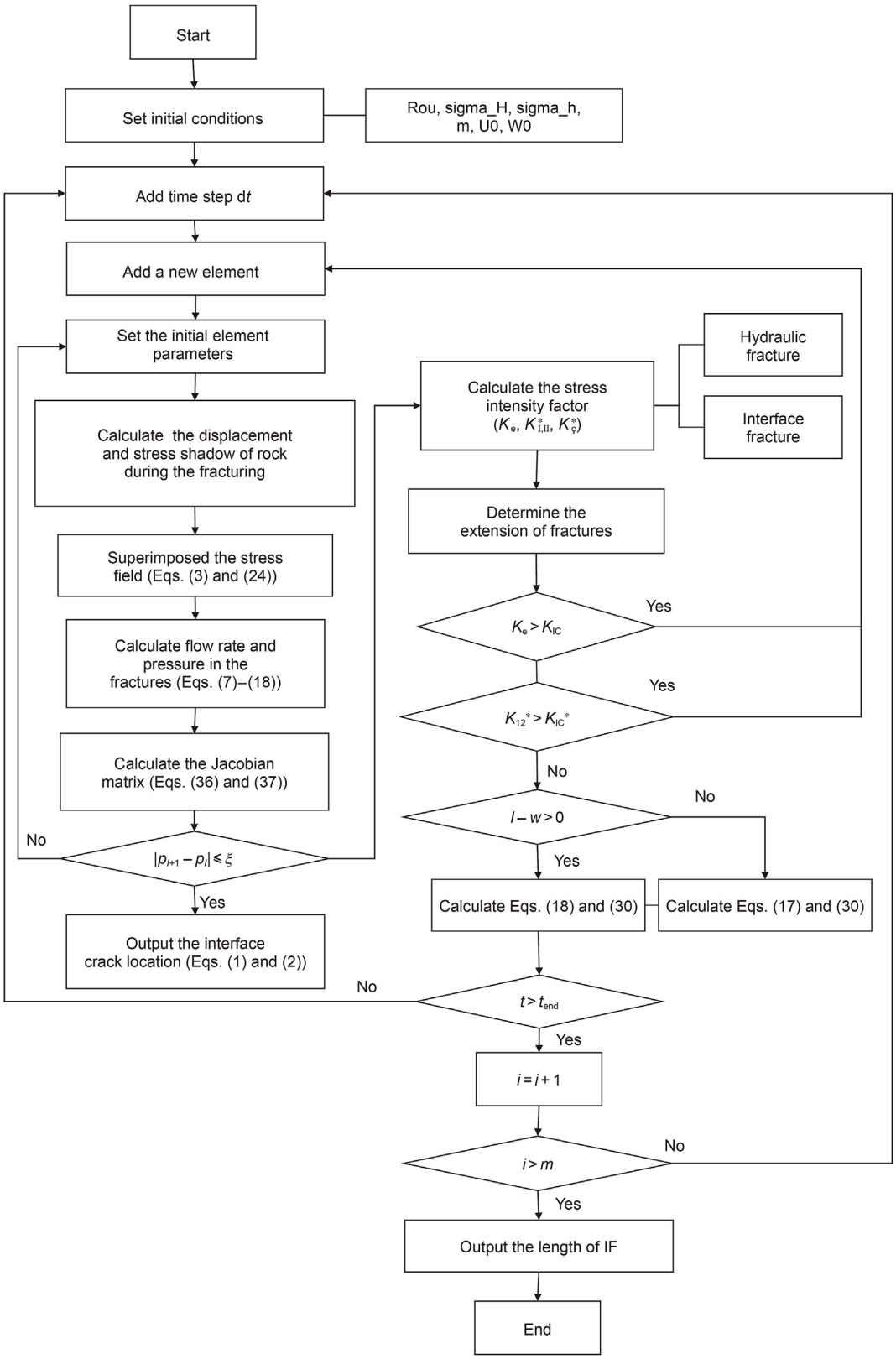

Fig. 3. Flow chart of the model solution.

fracturing each section can be obtained.

The Newton–Raphson method is used to calculate the nonlinear equations with a fully coupled iterative approach. Fig. 3 shows the specific solution process. Firstly, the initial conditions such as the formation conditions, fracturing parameters (pressure and displacement) and wellbore radius were set, the time step and units of Stage 1 were added. The displacement, pressure, and flow distribution of each fracture element are calculated using the rock deformation equation and fluid flow equation. If the difference between the new pressure and the initial value is less than the convergence accuracy $\xi = 0.005$ MPa (Cong et al., 2021), perform the next calculation step; otherwise, update the initial value. The position of the IF (CCI or CFI) is judged according to the obtained pressure in the fracture. The stress intensity factors of the HF and IF are calculated, and whether the fracture expands is judged. If it extends, enter the next time step; if it does not expand, further judge whether the IF is connected in the stage, and calculate the length of the IFs on both sides of the fracturing section. When the time at which each fracture stops expanding reaches the pre-set fracturing construction time, the calculations for Stage 1 have been completed. Judge whether the number of stages meets the construction requirements. If not, carry out the fracturing calculations for the next stage. At this time, it should be noted that when calculating the shape of the HF and IF, the initial stress field should be superimposed with the stress shadow obtained during the last fracturing event. When the calculation reaches the number of stages required by the construction, output the IF length of each stage, and end the calculation.

2.5. Model validation

Since there have been few studies of the synchronous propagation of hydraulic fractures and interfacial fractures in the process of hydraulic fracturing, to verify the accuracy of the established models used in this work, the stress shadow during the propagation of multiple fractures, the propagation processes of main fractures and interfacial fractures are verified separately in this section.

2.5.1. Stress shadow

Sneddon and Elliot (1946) established the induced stress field model around a single fracture in one stage based on the calculation model of 2D elasticity theory (see Fig. 4(a)). On the basis, the superimposed induced stress model for the expansion of three clusters of fractures in the stage can be obtained (take the direction of wellbore along the direction of minimum horizontal principal stress as an example), as shown in Fig. 4(b):

The hole size was set as 215.9 mm, the fracture half-seam length was set as 50 m, the pressure in the fracture was set as constant 1 MPa, the horizontal principal stress difference was set as 4 MPa, the rock Young's modulus was set as 30 GPa, and the Poisson's ratio was set as 0.2. The changes of the induced stress along the shaft in the x and y directions of wellbore are calculated, respectively, the results are shown in Fig. 5.

As shown in Fig. 5, when a single fracture expands, the closer to the fracture, the greater the induced stress, which is approximately equal to the net pressure. With the increase in the distance, the induced stress in the x and y directions decreases rapidly, and slowly decreases to 0 when the distance from the fracture is 1.5 times the fracture length. When three fractures spread together, the induced stress is about 3 times that of a single fracture expansion where the distance from the fracture is less than 0.5 times the length of the fracture. The ground stress distribution of the wellbore attachment will be affected, which will affect the fracture propagation of the next stage. The numerical solutions and analytical solutions of the induced stress in the x and y directions of single fracture and three fractures are all in good agreement, which proves that the DDM method can successfully calculate the induced stress field.

2.5.2. Validation of hydraulic fracture propagation

Detournay (2004) analysed the propagation of a KGD fracture and introduced a viscosity scaling appropriate for "small" toughness and a toughness scaling for "large" toughness. When the injected flow viscosity is dominant, assuming that the material toughness is 0, the hydraulic fracture propagation length is as follows:

$$L_{\mathrm{m}} = \left(\frac{E'Q^3t^4}{12\mu}\right)^{1/6} \tag{40}$$

with

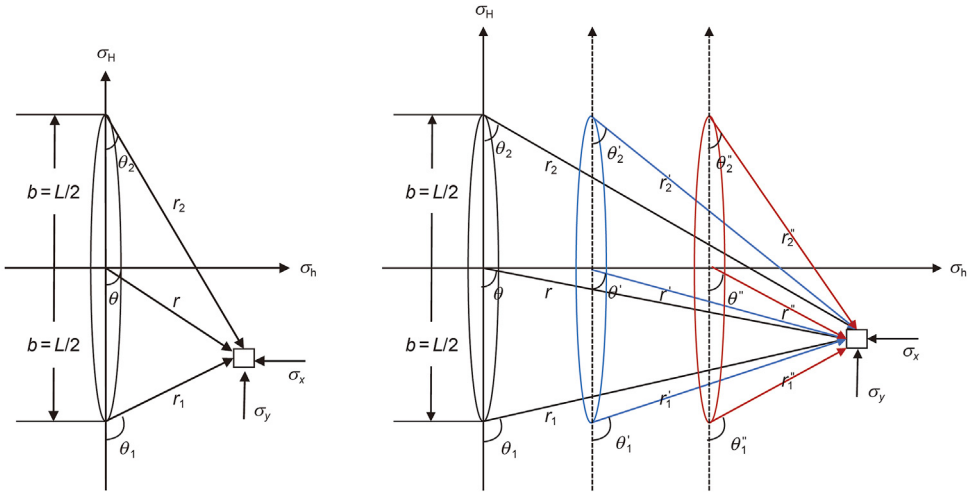

(a) Propagation of single-cluster fracture **(b)** Propagation of three-cluster fractures

Fig. 4. Geometric model of stress field induced by hydraulic fracture.

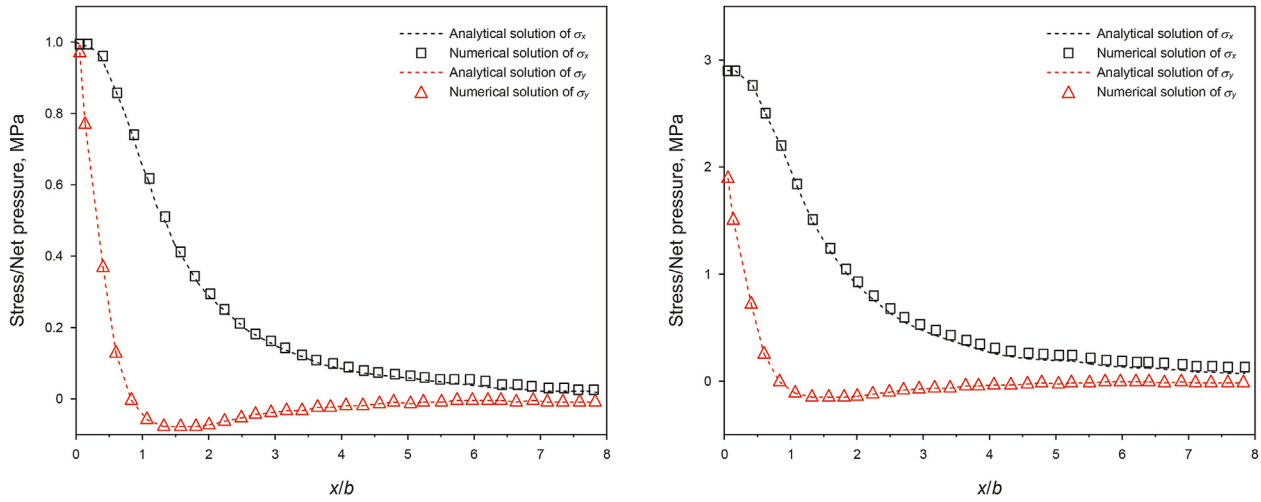

Fig. 5. The variation of hydraulic fracture induced stress in the x and y directions.

$$E' = \frac{E}{1-\nu^2}.$$

When the material toughness is dominant, assuming that the fluid viscosity is 0, the hydraulic fracture propagation length is as follows:

$$L_k = \left(\frac{EQt}{K'}\right)^{2/3} \tag{41}$$

The dominant conditions of hydraulic fractures can be determined using the following formula:

$$\kappa = \frac{K'}{\left(12E'^3\mu Q\right)^{1/4}} \tag{42}$$

where $K' = 4\left(\frac{2}{\pi}\right)^{1/2}K_{IC}$; if $\kappa \leq 1$, the propagation of hydraulic fractures is dominated by fluid viscosity (Garagash and Detournay, 2005); if $\kappa \geq 4$, the propagation of hydraulic fractures is dominated by toughness (Garagash, 2000).

The analytical solutions of fracture length under viscosity dominance and toughness dominance were used to verify the model. The calculated parameters are shown in Table 1, and the results are shown in Fig. 6.

The red solid and dotted lines represent the comparison results between the analytical and numerical solutions under viscosity dominance, and the final fracture length error is approximately 8.5%. The blue solid and dotted lines represent the comparison results between the analytical and numerical solutions under toughness dominance, and the error is approximately 13%. The overall trend is in good agreement. It is shown that the numerical model established in this paper has good applicability in simulating hydraulic fractures dominated by viscosity or toughness.

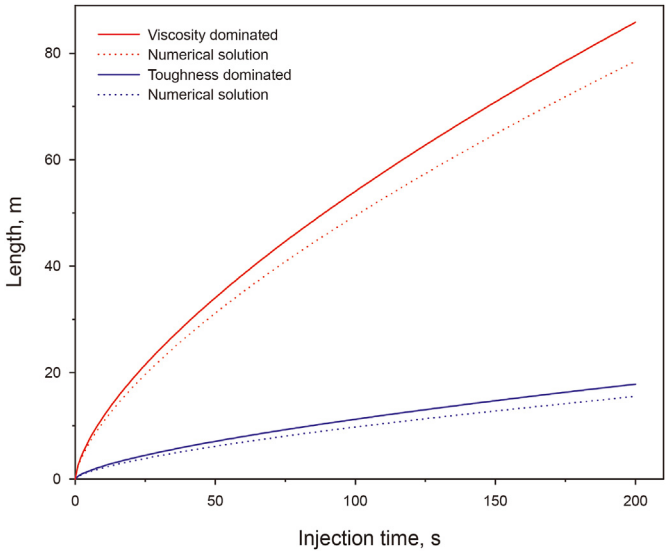

Fig. 6. Fracture length varies with time.

2.5.3. Validation of interface fracture propagation

The model is verified by the IF propagation experiment of Lecampion et al. (2013). Aluminium tubes, epoxy resin, and polymethylmethacrylate were used to simulate the casing, cement sheath, and formation. Water was pumped into the pre-set gap, and then the interface expansion process was recorded. The relevant basic parameters used in the simulation are shown in Table 2. Fig. 7 shows a comparison between the calculated results and the experimental results.

As shown in Fig. 7(a), the expansion of the IF increases synchronously along its circumference and slows with the passage of

Table 1
Parameters used in calculation.

E, GPa	Q, $m^2 \cdot s$	K_{IC}, $MPa \cdot m^{1/2}$	μ, $Pa \cdot s$	ν	κ	Dominant mechanism
30	0.001	1	0.01	0.25	0.403	Viscosity
6	0.001	5	0.001	0.15	12.367	Toughness

Table 2
Basic data for verification.

Parameter	Value	Parameter	Value
Casing thickness, mm	3	Inlet pressure, MPa	14
Inner casing radius, mm	14	Inner bore pressure, MPa	4
Outer casing radius, mm	22	Initial IF length, mm	3
Young's modulus of casing, GPa	69	Poisson's ratio of casing	0.33
Young's modulus of cement, GPa	2.5	Poisson's ratio of cement	0.35
Young's modulus of formation, GPa	3.3	Poisson's ratio of formation	0.35
Viscosity, Pa·s	11.9	K_{IC}, MPa·m$^{1/2}$	0.28
χ, GPa	2		

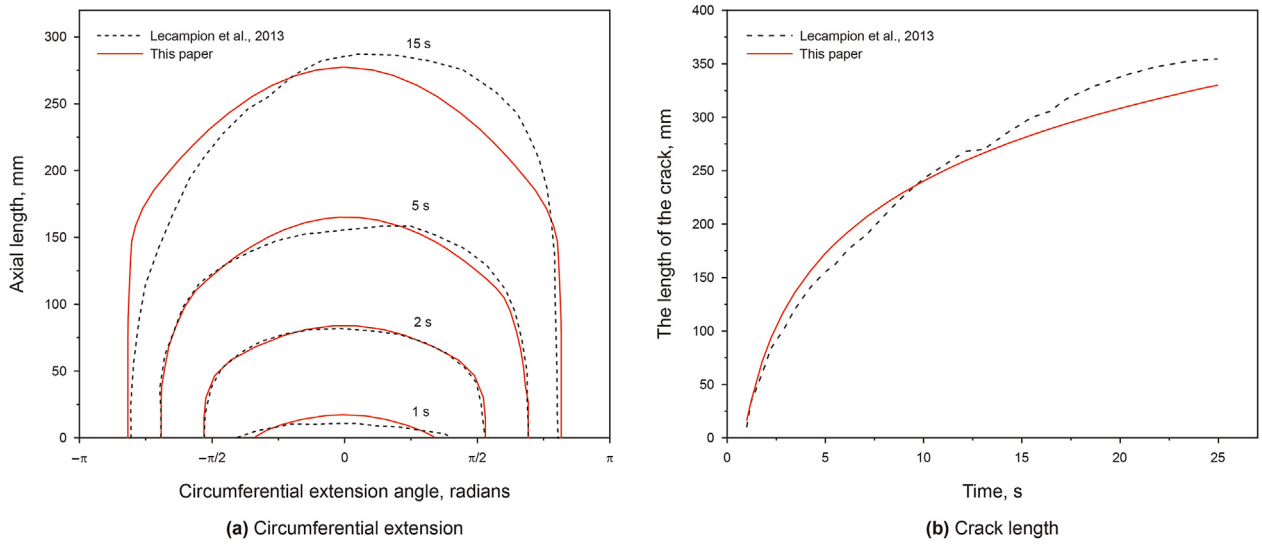

Fig. 7. Comparison of the fracture propagation morphology varying with time from the work of Lecampion et al. (2013) and the results of this paper.

time. The simulation results show that with the axial expansion of the IF, the circumferential expansion range does not cover the whole annulus but tends to a constant value. This is also consistent with the research results of Yan et al. (2020) because the friction of the fluid along the axis is much less than that along the circumferential flow of the wellbore, and the interfacial micro annular gap tends to expand in the vertical direction rather than in the circumferential direction. Fig. 7(b) shows that the average error and final relative error of the IF propagation length are 3.82% and 6.9%, respectively. The IF propagation trajectory matches well with the experimental results, which shows that the model established in this paper can successfully describe the propagation process of the IF. Compared with the experimental results, the simulation results are slightly smaller in the later stages of liquid injection, which are due to the limitation of liquid injection conditions and heterogeneity in the laboratory experiment. The fractures are not completely symmetrical, such that the maximum axial expansion length will be different when the injected fluid volume is the same. The discontinuities of the fracture tip displacement of the model in this paper are obtained by means of the stress field. The flow of fluid into the fracture and the increase in the fluid pressure inside the fracture are the premise of fracture propagation. To determine whether the fracture is expanding, the fluid–structure coupling process always meets the conservation of mass and energy, which means that the fluid always fills the fractures. Therefore, the fluid front curve was used as the verification object in the process of model verification. The experimental results show that the gap between the fluid front and the fracture front in the interface is small (less than 0.05 m). Although the experimental time scale is small, the growth of the fluid front and that of the fracture front are synchronous. Therefore, in the design of stage spacing, the fracture length gap due to the fluid hysteresis effect can be ignored.

3. Results

A schematic diagram of the model is shown in Fig. 8. The axis of the horizontal section extends along the direction of the minimum horizontal principal stress of the formation. The horizontal section is successively fractured in stages from right to left, assuming that the cement sheath remains intact in the subsequent sections during the first fracturing operation. The basic parameters are set with reference to the parameters of conventional fracturing wells. The geometric parameters and some fracturing parameters are fixed, the fracturing fluid flow rate varies with the number of clusters in the stage, and the flow rate of a single cluster is 2 $m^3 \cdot min^{-1}$. Then, the parameter values of one or two variables are different from the basic parameters used to analyse the interface connectivity under the conditions of various influencing factors (Table 3) and calculate the reasonable spacing of fracturing sections, where the values of K_{IC}^* and K_{IIC}^* are taken with reference to the study of Yang et al. (2009).

3.1. IF connectivity

In this section, the joint propagation process of HFs and IFs in the first four stages are analysed when three clusters of fractures exist in a given stage, as well as the propagation of IFs when four to six clusters of fractures are present in the same stage.

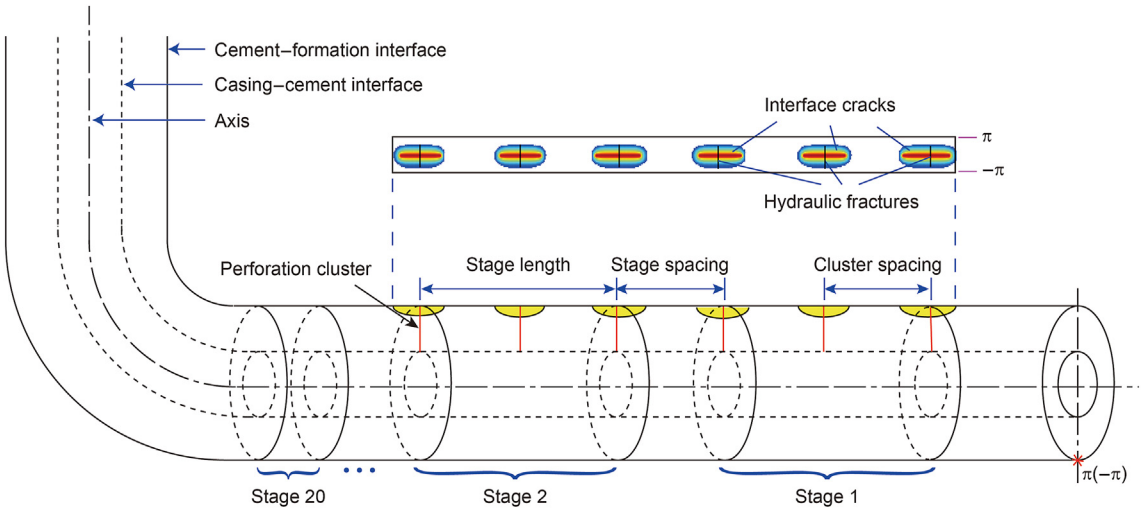

Fig. 8. Diagram of the geometric computational model.

Table 3
Fracture properties and material parameters.

Fixed parameter	Value	Fixed parameter	Value	Variable parameter	Value
Fracturing fluid rate, $m^3 \cdot min^{-1}$	6/8/10/12	Minimum horizontal *in-situ* stress, MPa	40.5	Cement Young's modulus, GPa	10
Well depth, m	3200	Fracturing fluid density, $g \cdot cm^{-3}$	1.1	Cluster spacing, m	15
Casing outer diameter, mm	139.7	Bore inner diameter, mm	215.9	Maximum horizontal *in-situ* stress, MPa	44.5
Bonding strength of CCI, MPa	1	Bonding strength of CFI, MPa	1	Rock Young's modulus, GPa	25
Cement Poisson's ratio	0.2	Rock Poisson's ratio	0.25	Number of clusters	3/4/5/6
Fluid power-law index	0.7	Consistency coefficient, $Pa \cdot s^n$	1.1		
Initial stage spacing, m	10	Initial stage length, m	30		
Initial HF length, m	5	Initial IF length, m	0.003		
K_{IC}^*, $Pa \cdot m^{1/2}$	0.25×10^6	K_{IIC}^*, $Pa \cdot m^{1/2}$	0.38×10^6		
K_{IC}, $Pa \cdot m^{1/2}$	1×10^6				

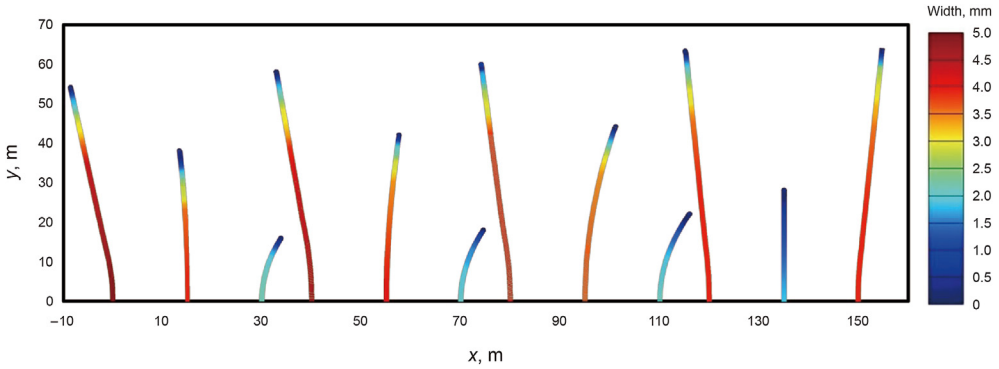

Fig. 9. Propagation path and morphology of HF in sequence.

3.1.1. Three clusters of fractures in the stage

According to the fluid–structure coupling calculation, the geometric morphology of HF propagation is shown in Fig. 9 after the first four stages have been successively fractured from right to left. After first fracturing, the shear stress fields generated by the HF tips on both sides are large due to the "stress shadow" effect, and the fracture propagation path presents an "exclusion" shape with the main fracture in the middle being the symmetry axis. The middle fracture suffered interference due to the stress of equal size and opposite direction, almost no shear stress was generated, and no deflection occurred. This is consistent with the conclusion of Zeng and Yao (2016). According to the flow distribution of HFs in each stage (Fig. 10), since the flow of the middle fracture is inhibited by the HFs on both sides, its length and width are smaller. Moreover, the width of the middle fracture gradually decreases from the heel of the fracture to the tip. The fracture length decreases from left to right in turn by comparing the fracture morphology in Stages 2 to 4. By comparing the fracture morphology at the corresponding positions of each stage, it is found that the fracture length decreases and the width increases, and the deflection angle increases on a stepwise basis. The HF on the left side of the stage always distributes the maximum flow, and the deflection direction of the middle HF changes from right to left. The HF on the right side in these stages has a poor propagation effect due to the presence of a stress

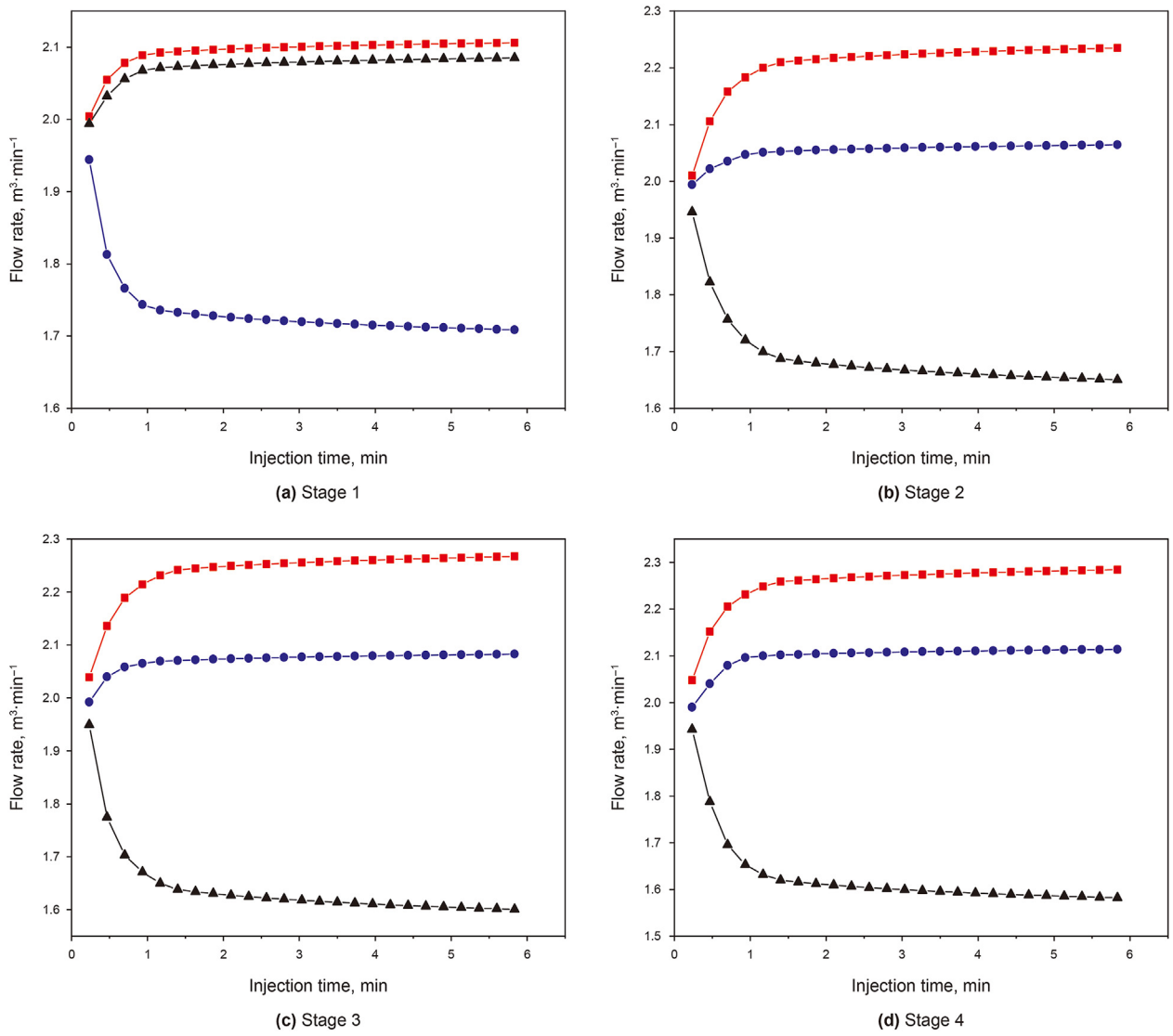

Fig. 10. Flow rate of three clusters in a stage during fracturing (the red, blue, and black curves show the hydraulic fracture flow rate from left to right).

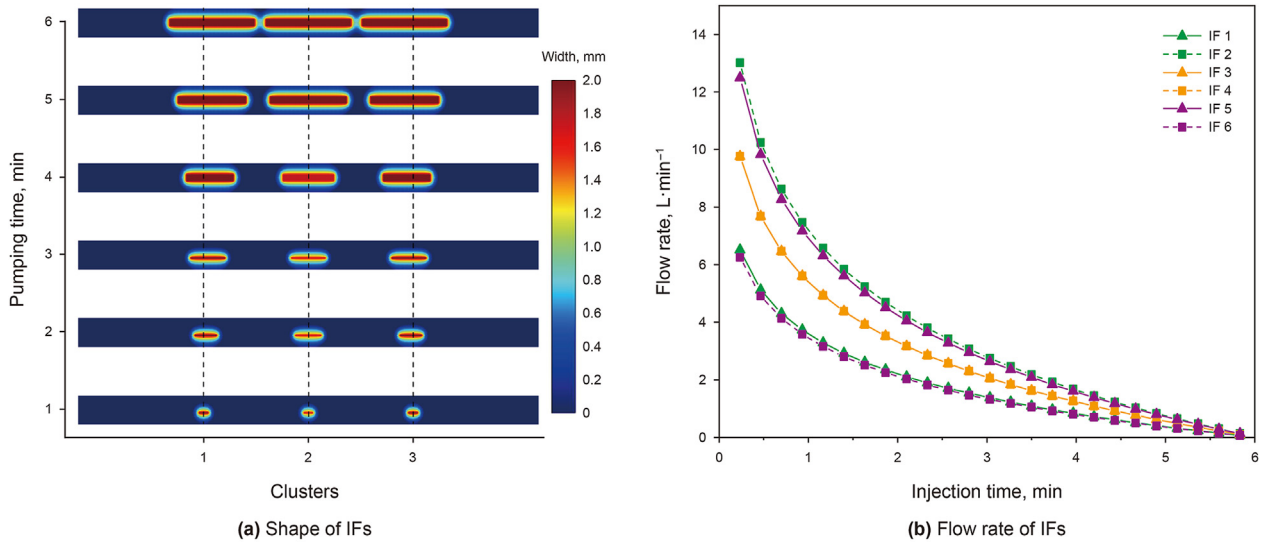

Fig. 11. IF propagation during the first stage of fracturing (the curves of IFs 1–6 show the interface fracture flow rate from left to right).

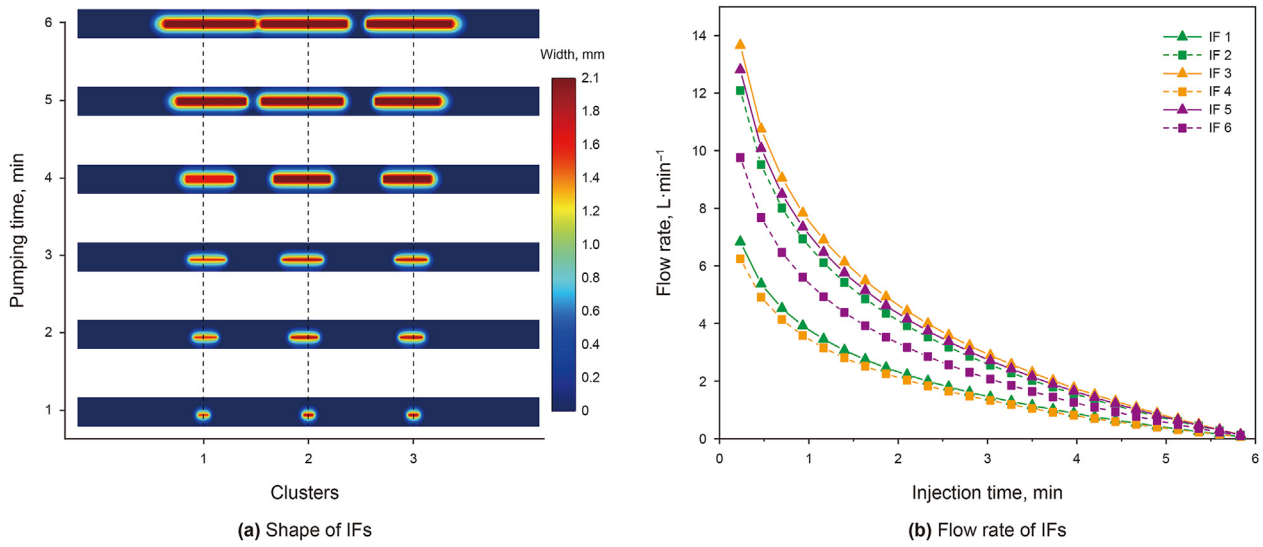

Fig. 12. IF propagation during the second stage of fracturing (the curves of IFs 1–6 show the interface fracture flow rate from left to right).

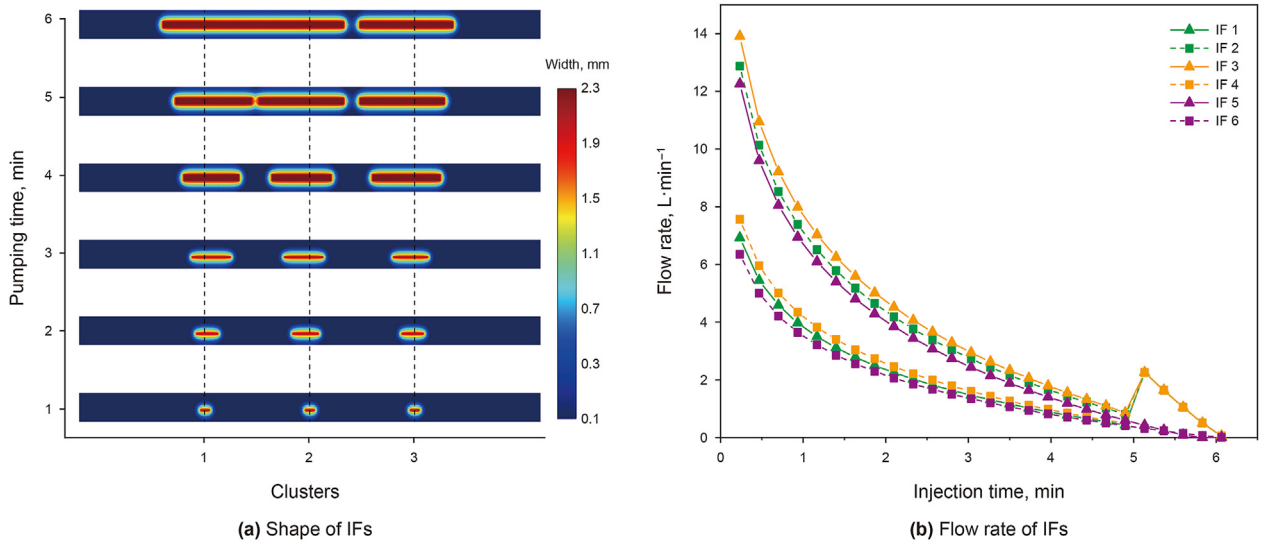

Fig. 13. IF propagation during the third stage of fracturing (the curves of IFs 1–6 show the interface fracture flow rate from left to right).

shadow.

The IF propagation phenomena on both sides of the three clusters of HFs in the first four stages are shown in Figs. 11–14. In Stage 1, the IFs take the middle HF as the axis and expand symmetrically (see Fig. 11(a)). With increasing fracturing time, the IFs on both sides of the first HF gradually show a trend of being short on the left and long on the right, while the third HF exhibits different behaviour. This shows that the IF is also affected by the "stress shadow." Due to the superposition of the propagation stress field, the IF between the HFs is easier to expand, and the length and width of the first and third HFs are greater than that of the second HF. This is because the flow of the middle HF is restrained by the HFs on both sides. Under the same conditions, the flow of the IFs near the middle HFs is less than that near the IFs on both sides. The propagation time of IFs is basically the same, and the propagation stops at approximately 5.8 min (see Fig. 11(b)).

As shown in Fig. 12(a), in Stage 2, the IF propagation presents different shapes relative to that in Stage 1 under the influence of the stress shadow, manifesting as the propagation length and width of the first IFs being the smallest while those of the middle IFs are the longest. With increasing fracturing time, the IFs of Cluster 2 and Cluster 3 are longer on the left and shorter on the right, which is caused by the superposition of the stress field and the competition of fracture fluid flow. Combined with the results of the flow distribution (Fig. 12(b)), more fluid flow is allocated to IF 2 and IF 3, which can be observed in the interface connectivity between the hydraulic fractures of Cluster 1 and Cluster 2. More fluid flow was distributed to the IFs in Stage 2 than in Stage 1, indicating that a larger interval is required to prevent IFs from connecting to the previous stage.

As shown in Fig. 13(a), the IFs between Cluster 1 and Cluster 2 are preferentially connected, and with the increase in stages, the connection speed also increases, indicating that the superposition of the stress field more easily promotes the expansion of IFs and that the expansion is connected to the side of the previous fracturing. Combined with the results of the flow distribution (Fig. 13(b)), additional fluid flow was always distributed to the IFs during the stage. With the injection of fracturing fluid, IF 2 and IF 3

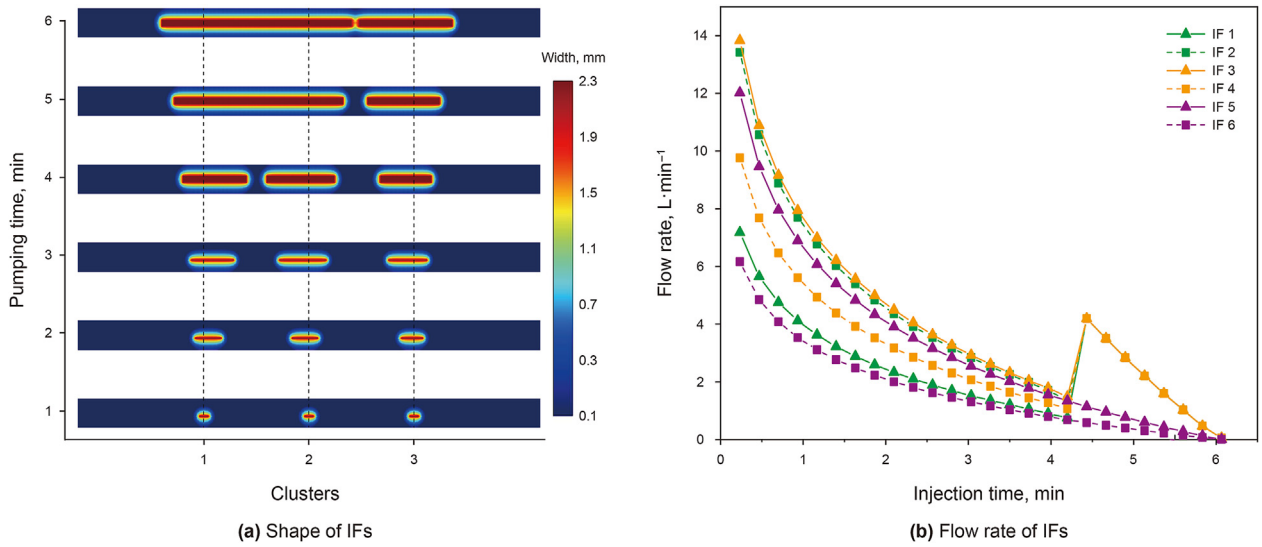

Fig. 14. IF propagation during the fourth stage of fracturing (the curves of IFs 1–6 show the interface fracture flow rate from left to right).

extend longer and gradually converge into a connected long IF at approximately 5.1 min.

The shape of the IFs in Fig. 14(a) is similar to that in Fig. 13(a), and the connection speed is further accelerated, with connection appearing at approximately 4.4 min. When IF 2 and IF 3 are connected, the fracture expands to both sides. In the same way, more fluid is distributed to the IFs and are more likely to be connected (Fig. 14(b)). The distribution of the fluid flow rate in all IFs is affected by the location and stage number, which presents nonlinear changes. Therefore, the required stage spacing between each stage is also nonuniform.

Fig. 15 shows the distribution of net pressure in the IFs on both sides of the stage during sequential fracturing. The net pressure and length of the IFs on both sides of the stage are basically the same as that in the first stage; with the sequential fracturing process, the net pressure at the fracture mouth on the left side increases slightly, while the net pressure on the right interface remains similar when the fracture length is shorter than 4.7 m and gradually increases when the fracture length surpasses 4.7 m. The fracture length on the left side of the stage is almost the same, while the fracture length on the right side of the stage gradually increases in the fracturing process, indicating that each stage requires greater spacing than the previous stage when considering the integrity of the wellbore.

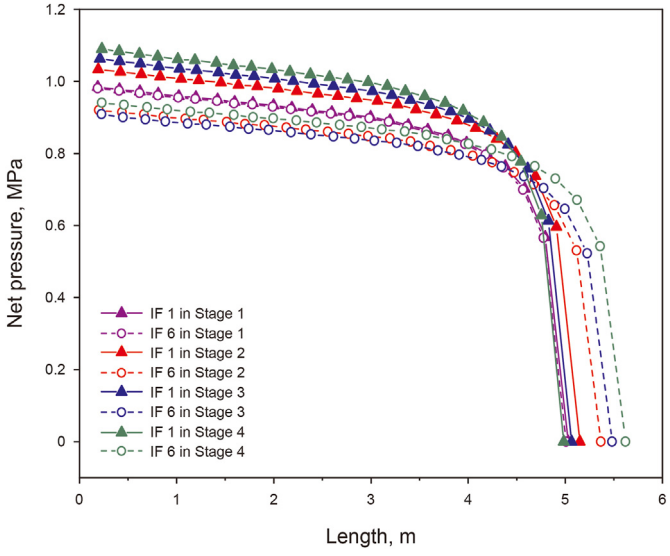

Fig. 15. The distribution of net pressure in the interfacial fracture with length.

3.1.2. Four clusters of fractures in the stage

Fig. 16 shows the IF propagation phenomenon caused by four clusters of HFs in the stage. Similar to the results in Fig. 11, in Stage 1, the IF also presents as axisymmetric expansion, and the expansion between clusters is easier to expand. The flow of the two clusters of HFs in the middle is restrained by the HFs on both sides, resulting in the extended length and increased width of the IFs on both sides relative to those of the middle fractures. During fracturing after Stage 2, as shown in Fig. 16(b), the IF near the previous stage is restrained by the stress shadow, the width is smaller than that of other fractures, and it gradually connects with the IF of its adjacent cluster. Fig. 16(c)–(d) shows that with increasing fracturing time, the IF begins to expand to both sides after it is fully connected in the stage and finally presents as being long on the left and short on the right. This asymmetric propagation effect leads to the need for an unequal stage spacing design to prevent channelling between fracture segments.

3.1.3. Five clusters of fractures in the stage

Fig. 17 shows the IF propagation phenomenon caused by five clusters of HFs in the stage. In Stage 1, the IF propagation forms a symmetrical propagation form with the third cluster of fractures as the axis. Similarly, the expansion trend of the HF can also be reflected by the width of the IF; that is, the HFs in Cluster 2 and Cluster 4 have the smallest flow and the shortest propagation length, which is consistent with the results of Cheng (2016). Therefore, the length and width of IFs on both sides are less than those of other fractures. With the increase in the stage number, the speed of interface connection gradually increases, and the IF close to the previous fracturing section is preferentially connected.

3.1.4. Six clusters of fractures in the stage

Fig. 18 shows the IF propagation phenomenon caused by six clusters of HFs in the stage. With the increase in fracturing time and the number of stages, the expansion trend is similar to that

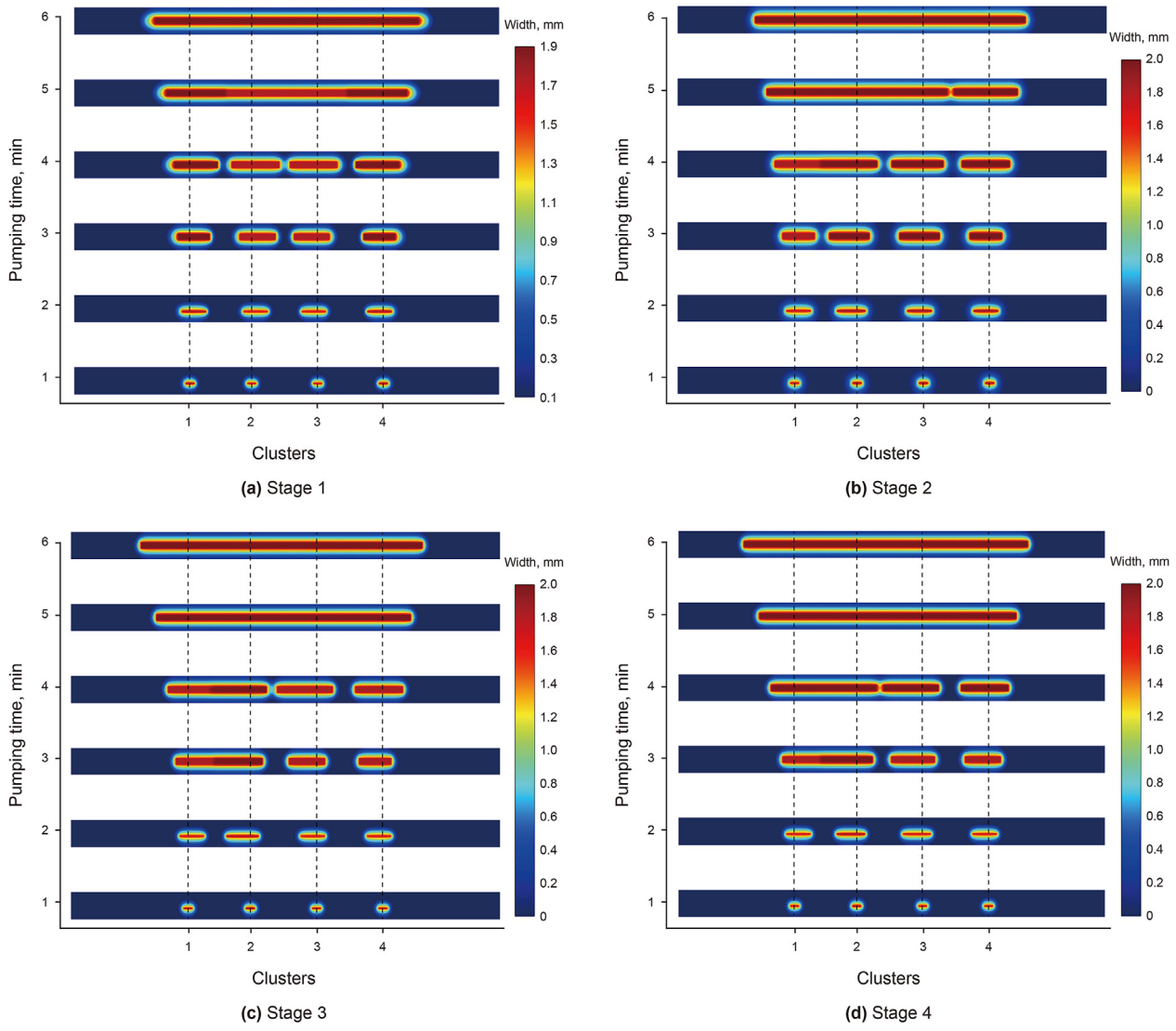

Fig. 16. Diagram of IF propagation with four clusters in a stage.

mentioned above. However, after the IFs are connected, the extension length to both sides of the stage gradually increases, which also shows that the increase in the number of fracturing clusters leads to the need for a larger spacing in each fracturing section than that in the previous stage.

3.2. Influencing factors of minimum stage spacing required (MSSR) of fracturing

The calculation results in the previous sections show that all IFs occur at the CFI. Consistent with the conclusion of Yin et al. (2019), this is because the Young's modulus of the casing is much larger than that of the formation, resulting in greater radial compressive stress at the CCI during loading, which hinders the system's ability to form a fluid migration channel. All fractures in this section are located at the CFI.

3.2.1. Number of fracturing clusters

The length of the stage is fixed, and the number of fracturing clusters is set to 3, 4, 5, and 6 to obtain the MSSR to prevent channelling. The simulation results are shown in Fig. 19. With a certain number of fracturing clusters, the MSSR between each stage and the previous stage gradually increases with the increase in stages. For example, when there are three clusters of fractures in a stage, the MSSR for Stage 2 is approximately 10.39 m and that for Stage 20 is 12.6 m. With the increase in the number of fracturing clusters, the MSSR and the increased range become more apparent, increasing slightly exponentially. When there are six clusters of fractures, the MSSR for Stage 2 fracturing is approximately 11.74 m, and the minimum interval required for Stage 20 is 28.29 m. This is because with the increase in stage, the superposition of the previous fractures and the initial stress field has a significant impact on the IF propagation. Under the condition of tighter cluster fracturing, increasing the number of HFs increases the propagation length of IFs and gradually aggravates the risk of channelling between stages. Therefore, with the progress of fracturing construction, a longer fracturing interval is required than the previous fracturing events. In addition, an escalation point is observed for the MSSR for Stage 2 and Stage 3 because in the first fracturing, the HFs and IFs spread symmetrically with the middle fracture as the axis, and the propagation length of the unilateral IF in the direction of Stage 1 (the MSSR between Stage 1 and Stage 2) is only affected by the number of HF clusters in the current stage (or the elastic modulus of the cement sheath and formation, etc.) in regard to the competitive

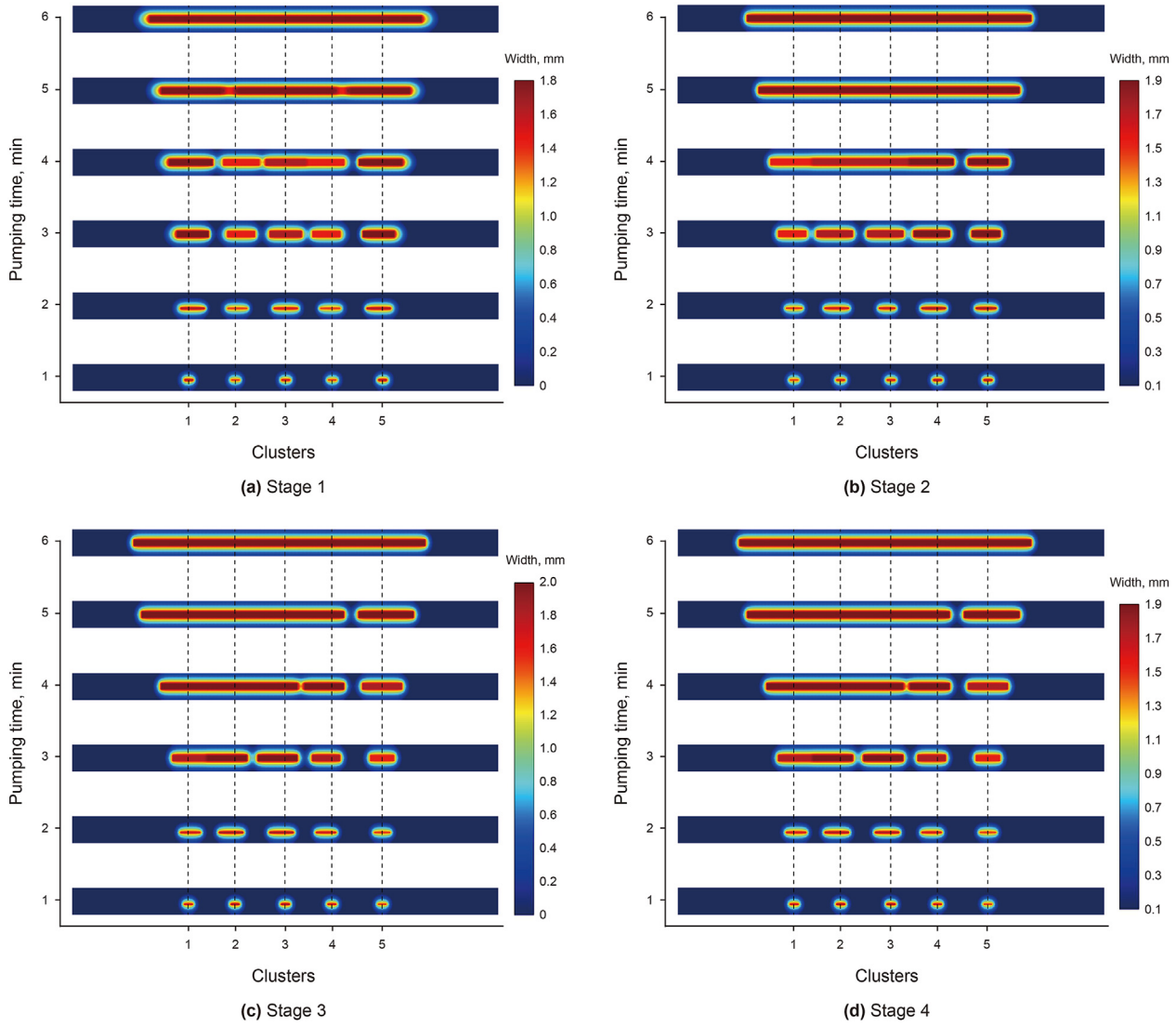

Fig. 17. Diagram of IF propagation with five clusters in a stage.

process of fracture propagation. In Stage 2, the stress shadow generated by the previous HFs in the process of competitive fracture propagation causes a large difference in the length of IF propagation; as a result, the MSSR for Stage 3 (the kick point) increases significantly. In the subsequent stages, the IF propagation is affected by the superimposed stress field formed by the previous HFs, so the fracture propagation length increases successively. Similarly, there are corresponding escalation points in the analysis of other influencing factors, the reasons for which are not reiterated.

3.2.2. Cluster spacing in the fracturing section

The number of fracturing clusters is fixed as three, and the cluster spacing is set as 5–25 m. The simulation results of the MSSR are shown in Fig. 20. With the increase in cluster spacing, the MSSR of each stage and the previous stage decreases significantly and tends to a constant value. When the cluster spacing increases from 5 to 15 m, the IF propagation length is significantly affected by the cluster spacing because the IF is easier to expand after being subjected to the obvious stress shadow effect. When the cluster spacing exceeds 15 m, due to the reduction in the stress shadow effect, the propagation length of IFs on both sides of the stage no longer shows a nonuniform trend but tends to expand symmetrically. At this time, the MSSR between fracturing sections also tends to a constant value, with an average value of approximately 10.67 m.

3.2.3. Young's modulus of cement sheath

The Young's modulus of the formation was fixed, and the Young's modulus of the cement sheath was set to 5–30 GPa. The simulation results of the MSSR are shown in Fig. 21. The MSSR for each stage increases with increasing Young's modulus of the cement sheath. When the Young's modulus of the cement sheath varies from 10 to 20 GPa, the increase in the MSSR is significantly greater than that in other intervals. The interface with a cement sheath with a low Young's modulus (<10 GPa) bears less radial pressure, which helps to protect the integrity of the interface, reduce the propagation length of IFs, and alleviate the superposition effect of the stress shadow after multistage fracturing. A cement sheath with a high Young's modulus (>20 GPa) leads to a large interface radial pressure, aggravates IF propagation, and significantly increases the minimum interval required for fracturing. However, due to the flow competition between the HFs and the IFs, the length of the IF is much smaller than that of the HF, and

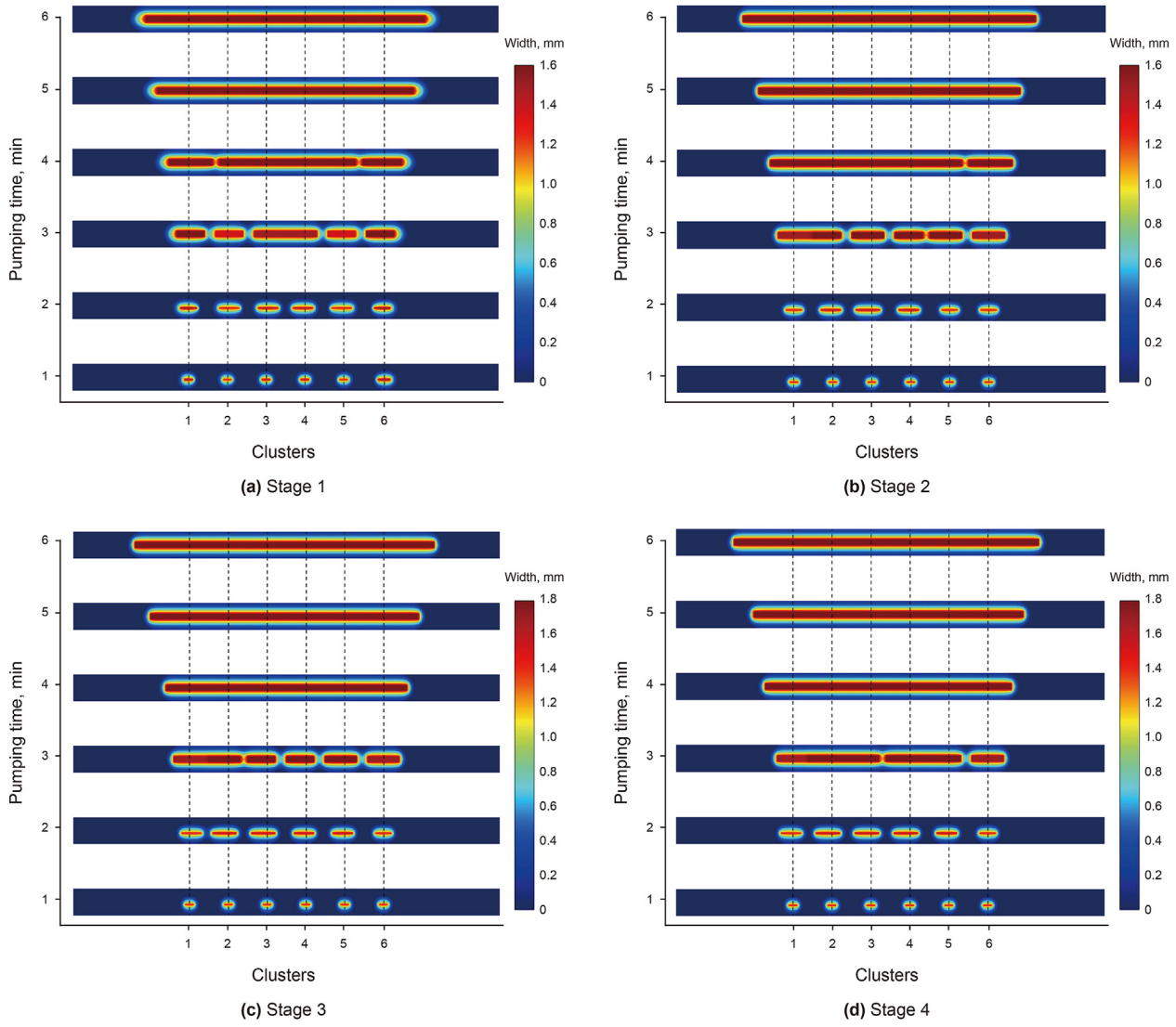

Fig. 18. Diagram of IF propagation with six clusters in a stage.

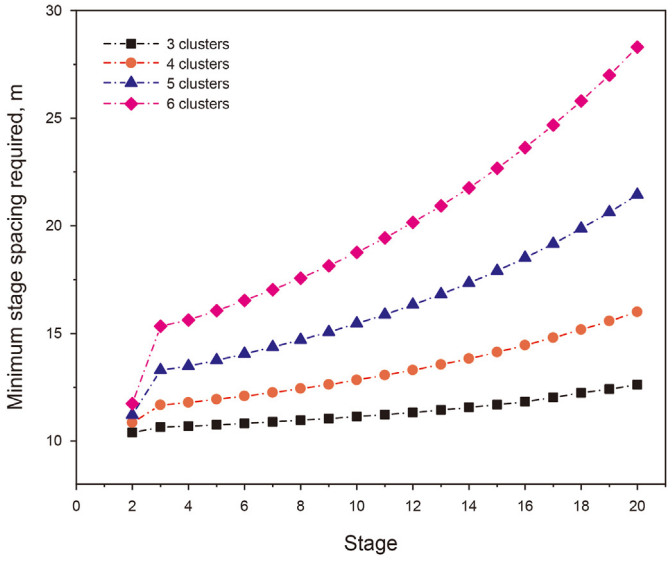

Fig. 19. Influence of fracturing cluster number on minimum required stage spacing.

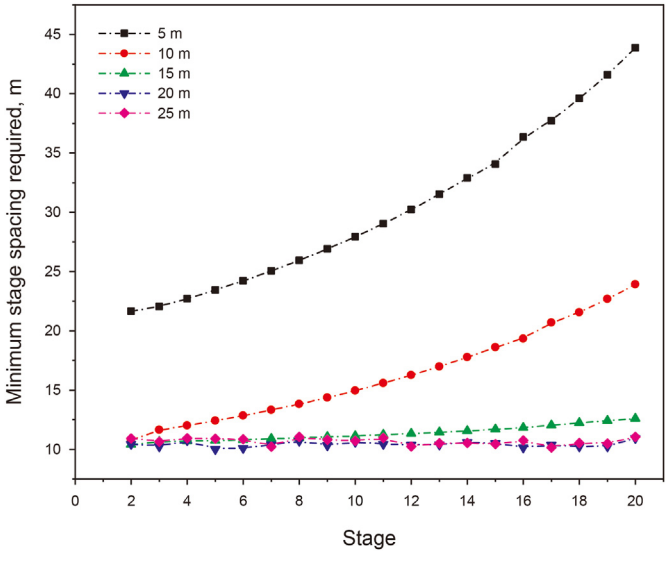

Fig. 20. Influence of cluster spacing on MSSR.

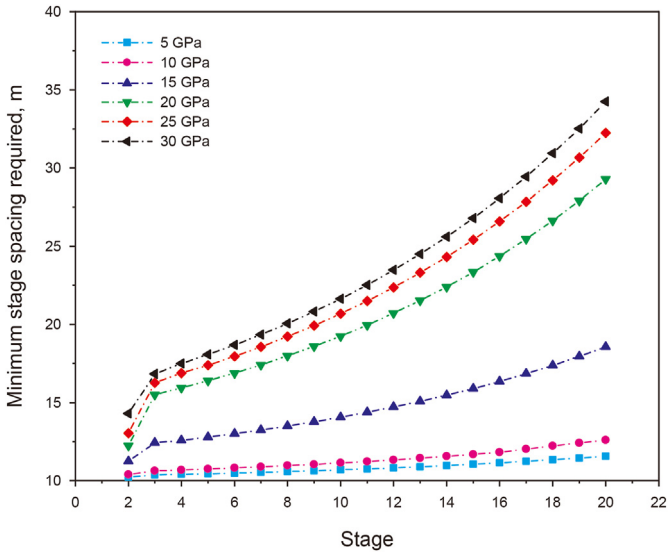

Fig. 21. Influence of Young's modulus of the cement sheath on the MSSR.

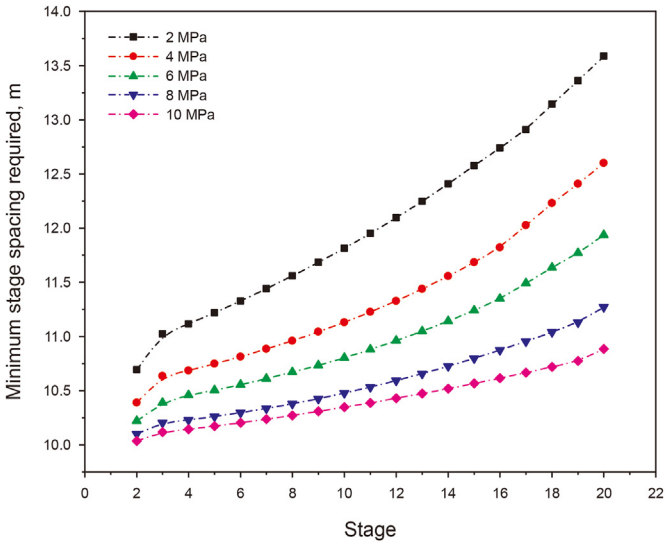

Fig. 23. Influence of the horizontal stress difference on the minimum required stage spacing.

its propagation length tends to a constant value. After several stages of fracturing, the increase in the MSSR decreased. Therefore, controlling the lower Young's modulus of the cement sheath is conducive to inhibiting the propagation of IFs and reducing the MSSR.

3.2.4. Young's modulus of formation

Fixing the Young's modulus of the cement sheath and setting that of the formation to 15–40 GPa, the simulation results of the MSSR to prevent channelling between segments are shown in Fig. 22. With the increase in the formation Young's modulus, the MSSR for fracturing at all stages increases, and the amplification increases significantly when the formation Young's modulus exceeds 25 GPa.

3.2.5. Horizontal principal stress difference

The minimum horizontal principal stress value is fixed, and the maximum horizontal principal stress is set to 42.5–50.5 MPa to correspond to the horizontal principal stress difference of 2–10 MPa. The simulation results of the MSSR are shown in Fig. 23. When Stage 20 is fracturing, the MSSR corresponding to different horizontal principal stress differences varies between 10.6 and 13.58 m, which shows that the horizontal principal stress difference has less effect on the MSSR than the factors mentioned above. With the increase in the horizontal principal stress difference, the MSSR for stage decreases, and the decrease gradually grows gentler under the same amplitude of stress difference. This is because the larger the horizontal principal stress difference is, the more conducive it is for HFs to overcome the stress shadow and expand along the direction of the maximum horizontal principal stress. Under the same stress field conditions, it becomes gradually more difficult for IFs on both sides of the stage to expand, so the corresponding stage spacing can be reduced.

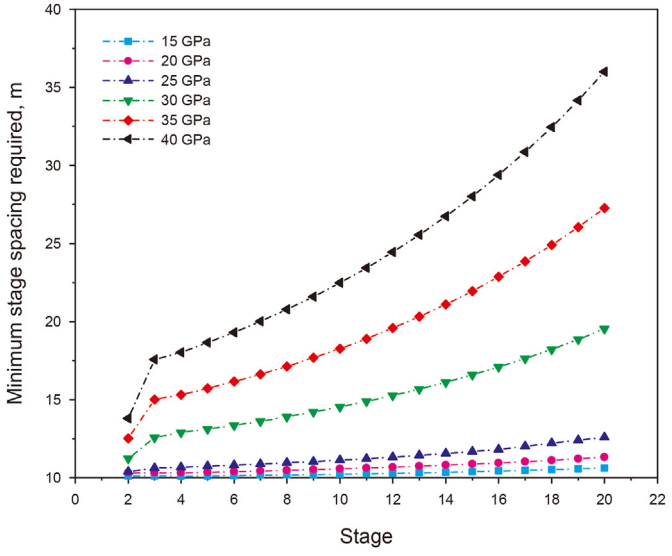

Fig. 22. Influence of the Young's modulus of formation on the MSSR.

3.3. Application examples

The reservoir depth of a shale oil fracturing block is approximately 3170 m in Xinjiang, China, and the horizontal principal stress difference is approximately 13.5 MPa. The length of the horizontal section of well X1 is designed to be 482 m, 14 stages are designed for fracturing, the length of the average stage spacing is 28 m, and there is 3–6 clusters of single section perforations. The specific fracturing scheme and relevant parameters are shown in Figs. 24 and 25 and Table 4, and the rheological parameters of the fracturing fluid and fracture toughness are the same as those in Table 3.

The MSSR for the well is calculated and compared with the actual interval. The results are shown in Fig. 26. It shows the length of IFs on the left and right sides of each stage in the fracturing process of 14 stages, and the sum of the length of the left crack in the previous stage and the length of the right crack in the next stage is the MSSR. The difference in the number and displacement of fracturing clusters in each stage leads to the different propagation lengths of IFs between each stage, which vary between 10.36 and 14.46 m. The actual stage spacing fluctuates between 7 and 11 m, with an average of 7.38 m. The actual intervals are less than the theoretical calculation value, so its interface will be completely connected. If the length of the horizontal fracturing section can be

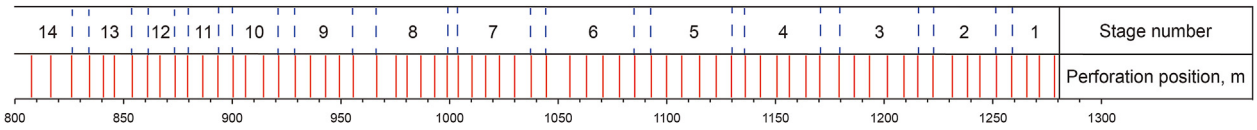

Fig. 24. Fracturing cluster design for the horizontal section of well X1.

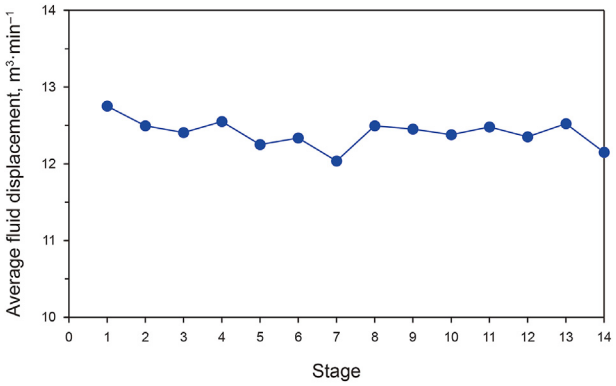

Fig. 25. Fracturing fluid rate curve of the pump.

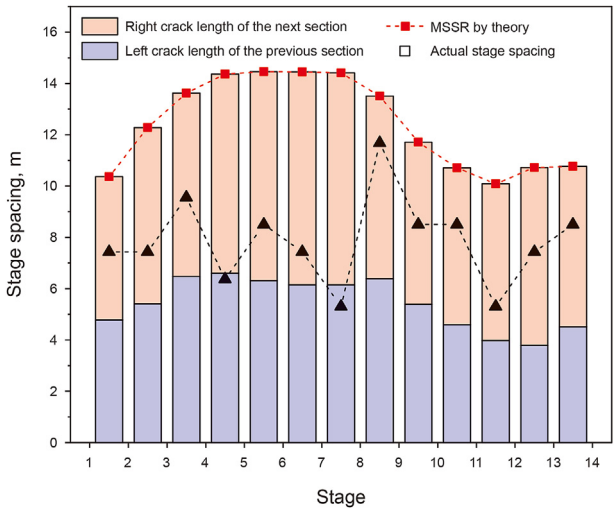

Fig. 26. The original and optimized design results of the stage spacing.

extended and the spacing can be adjusted, the risk of channelling caused by interface connection can be effectively prevented.

4. Discussion

In previous studies, almost all the optimization principles of stage spacing are to adjust the deflection angle of hydraulic fractures to obtain the maximum sweep area of fracture network, or to avoid the effect of adjacent fractures on stress interference. In this paper, starting from wellbore integrity, we continue the research idea of DDM, combine the fracture mechanics theory of dual-material interface, and use the flow–solid coupling model to realize the numerical simulation of co-extension of planar 2D hydraulic fracture and non-planar 3D solid interface fracture, the length of IF that fits the actual situation is obtained, the non-uniform stage spacing is optimized on this basis.

Due to the study perspective and the model established in this paper are relatively new, there are inevitably some problems that are different from the actual working conditions while idealization. Most of the existing models for hydraulic fracture propagation consider the fluid filtration condition. With the fracturing fluid filtration and subsequent fracturing, the HFs and IFs will be closed. However, this research does not consider this process, which mainly lies in two aspects: (1) Different from synchronous parallel propagation of HFs (without considering stress shadow), IFs will expand along the cementing interface, this may cause the closed IF to reopen, but the model established in this paper cannot simulate this situation temporarily, only the equivalent IF length can be calculated. (2) The research object of this paper is low permeability reservoir, ignoring fluid filtration (that is, the fluid will always exist in the fracture), the premise of this research is that the fractures won't be closed. The model established in this paper is the joint expansion of mutually vertical fractures, which is more complex than the solution of multiple hydraulic fractures, and the interface fractures are equivalent to nonplanar 3D fractures of circular arc shape, which will bring more difficulties when considering the fluid filtration. Therefore, this paper neglects the fluid leak-off during fracture propagation based on the principle of risk maximization, and further research still needs to be improved on fracture closure conditions.

In addition, increasing the cementing strength or reducing the inlet pressure in fractures can prevent the IFs from expanding on the basis of the established fracture propagation model of the cementing interface. However, there are some limitations in optimizing fracturing parameters. For example, there is a lack of quantitative data to support the research on the correlation between the fracture toughness of the cement sheath interface and its bonding strength; fracture toughness of IF is far less than that of HF. Reducing the inlet pressure will greatly affect the expansion of HF. Therefore, the current research in this paper cannot perfectly solve the above problems and is only applicable to the optimization of stage spacing under fixed parameters. How to judge the advantages and disadvantages of each fracturing operation parameter on the joint expansion of IFs and HFs, and form a parameter matching scheme to maximize benefits is the next problem to be improved.

Table 4
Parameters of wellbore and fracturing.

Fixed parameter	Value	Fixed parameter	Value
Fracturing fluid rate, $m^3 \cdot min^{-1}$	12–14	Fracturing fluid density, $g \cdot cm^{-3}$	1.1
Casing outer diameter, mm	139.7	Bore inner diameter, mm	215.9
Bonding strength of CCI, MPa	1.4	Bonding strength of CFI, MPa	0.78
Cement Poisson's ratio	0.2	Rock Poisson's ratio	0.25
Cement Young's modulus, GPa	14.5	Rock Young's modulus, GPa	27.6

5. Conclusions and suggestions

Based on bimaterial IF propagation theory and the multiple fracture propagation competition mechanism, a calculation model of the IF length is established, and an unequal stage spacing optimization model is proposed that considers the integrity of the wellbore interface after fracturing. The conclusions are as follows:

(1) When each HF in Stage 1 expands, the IFs expand symmetrically with the central point in the stage taken as the axis. The IFs are connected in the stage first and then expand along both sides.
(2) In Stage 2 fracturing and subsequent, the IFs of each cluster expand asymmetrically left and right, and two types of expansion behaviour are present: one is expansion and connection in the stage first, and the other is expansion in the direction close to the previous stage first, which depends on the joint effect of stress shadow and flow competition in the process of HF expansion.
(3) In Stage 2 fracturing and subsequent, after the interface is connected, the IFs on both sides of the stage expand towards the side of the previous stage, and the difference in the expansion length of the interface on both sides increases with the increase in the stage number.
(4) The MSSR for fracturing is positively correlated with the number of fractures in a stage, and the Young's moduli of the cement sheath and formation are negatively correlated with the cluster spacing and horizontal principal stress difference. The influence of the horizontal principal stress difference on the MSSR is less than that of the other factors.
(5) The sensitivity of IF propagation is the strongest when the Young's modulus of the cement sheath is 10–20 GPa. Under the condition that other factors cannot be changed, restricting the Young's modulus of the cement sheath to less than 10 GPa can effectively shorten the MSSR.

Since the purpose of hydraulic fracturing is to form a complex fracture net in the reservoir and improve the production of oil and gas wells, a stage spacing that is too large reduces the utilization rate of horizontal well sections, and the existing fracturing interval optimization methods are based on the principle of maximum reconstruction volume. From the perspective of wellbore integrity, this paper delivers a minimum stage spacing optimization method to prevent channelling risk. Combining this paper with the existing methods to further determine the appropriate stage spacing and maintain the wellbore integrity without reducing the effective development rate of the reservoir is of great significance for the later production of oil and gas resources and the maintenance of wellbore life. This also is constituting the direction of the author's future research.

Declaration of competing interest

The authors declare that they have no known competing financial interests or personal relationships that could have appeared to influence the work reported in this paper.

Acknowledgements

This work was supported by the Natural Science Foundation of Heilongjiang Province of China (YQ2021E005), the National Natural Science Foundation of China (No.51774094), the Youth Fund Project of National Natural Science Foundation of China (52004065), the Heilongjiang Natural Science Foundation Project (excellent youth project) (YQ2021E006), "Reveal the top" Science and Technology Project of Heilongjiang Province (2021ZZ10-04).

Appendix A

This appendix shows the expressions of Eq. (2)

$$f_1 = \frac{1+\nu_1}{E_1}\frac{2(1-\nu_1)r_1^2 r_2}{r_2^2 - r_1^2}$$

$$f_2 = \frac{1+\nu_1}{E_1}\frac{r_1^2 r_2 + (1-2\nu_1)r_2^3}{r_2^2 - r_1^2}$$

$$f_3 = \frac{1+\nu_2}{E_2}\frac{r_2^2 r_3 + (1-2\nu_2)r_2^3}{r_3^2 - r_2^2}$$

$$f_4 = \frac{1+\nu_2}{E_2}\frac{2(1-\nu_2)r_3^2 r_2}{r_3^2 - r_2^2}$$

$$f_5 = \frac{1+\nu_2}{E_2}\frac{2(1-\nu_2)r_2^2 r_3}{r_3^2 - r_2^2}$$

$$f_6 = \frac{1+\nu_2}{E_2}\frac{r_2^2 r_3 + (1-2\nu_2)r_3^3}{r_3^2 - r_2^2}$$

$$f_7 = \frac{1+\nu_3}{E_3}\frac{r_3^2 r_o + (1-2\nu_3)r_3^3}{r_o^2 - r_3^2}$$

$$f_8 = \frac{1+\nu_3}{E_3}\frac{2(1-\nu_3)r_3 r_o^2}{r_o^2 - r_3^2}$$

where E_1, E_2, and E_3 are the Young's moduli of the casing, cement sheath, and formation, respectively, Pa; ν_1, ν_2, and ν_3 are the Poisson's ratios of casing, cement sheath, and formation, respectively; and r_1, r_2, r_3, and r_o are the radii of the inner casing wall, CCI, CFI, and outer formation, m.

References

Adams, N.J., Mitchell, R.F., Eustes, A.W., Sampaio, J.H., Antonio, A.O., 2017. A causation investigation for observed casing failures occurring during fracturing operations. In: SPE Hydraulic Fracturing Technology Conference & Exhibition. https://doi.org/10.2118/184868-MS.

Al-Rbeawi, S., 2019. An approach for the performance-impact of parent–child wellbores spacing and hydraulic fractures cluster spacing in conventional and unconventional reservoirs. J. Petrol. Sci. Eng. 185, 106570. https://doi.org/10.1016/j.petrol.2019.106570.

Batchelor, G.K., 1967. An Introduction to Fluid Dynamics. Cambridge University Press, Cambridge.

Bois, A.P., Gamier, A., Galdiolo, G., Laudet, J.B., 2012. Use of a mechanistic model to forecast cement-sheath integrity. SPE Drill. Complet. 27 (2), 303–314. https://doi.org/10.2118/139668-PA.

Chen, X.Y., Zhao, J.Z., Li, W.Y., Zhang, X., 2019. Numerical simulation of simultaneous hydraulic fracture growth within a rock layer: implications for stimulation of low-permeability reservoirs. J. Geophys. Res. Solid Earth 124 (12), 13227–13249. https://doi.org/10.1029/2019JB017942.

Chen, Z.R., Bunger, A.P., Zhang, X., Robert, G.J., 2009. Cohesive zone finite element-based modelling of hydraulic fractures. Acta Mech. Solida Sin. 22 (5), 443–452. https://doi.org/10.1016/S0894-9166(09)60295-0.

Cheng, W., 2016. Mechanism of Hydraulic Fracture Propagation in Fractured Shale Reservoir in Three-Dimensional Space. Ph.D. Dissertation. China University of Petroleum, Beijing (in Chinese).

Chu, W., Shen, J.Y., Yang, Y.F., Li, Y., Gao, D., 2015. Calculation of microannulus size in casing-cement sheath-formation system under continuous internal casing pressure change. Petrol. Explor. Dev. 42 (3), 414–421. https://doi.org/10.1016/S1876-3804(15)30033-1.

Cong, Z.Y., Li, Y.W., Liu, Y., Xiao, Y.H., 2021. A new method for calculating the direction of fracture propagation by stress numerical search based on the displacement discontinuity method. Comput. Geotech. 140, 104482. https://doi.org/10.1016/j.compgeo.2021.104482.

Cong, Z.Y., Li, Y.W., Pan, Y.S., Liu, B., Shi, Y., Wei, J.G., Li, W., 2022. Study on CO_2 foam fracturing model and fracture propagation simulation. Energy 238, 121778. https://doi.org/10.1016/j.energy.2021.121778.

Conrod, C.L., Yin, Y.B., Hanna, T., Atkinson, A.J., Alvarez, P.J.J., Tekavec, T.N., Reynolds, M.A., Wong, M.S., 2020. Fit-for-purpose treatment goals for produced

waters in shale oil and gas fields. Water Res. 173, 115467. https://doi.org/10.1016/j.watres.2020.115467.
Deng, K.H., Xie, P.F., Yuan, Y., Zeng, D.Z., Li, Q., Lin, Y.H., 2021. Study on the effect of interface failure between casing and cement sheath on casing stress under nonuniform in situ stress. Appl. Math. Model. 91 (3), 632–652. https://doi.org/10.1016/j.apm.2020.10.007.
Detournay, E., 2004. Propagation regimes of fluid-driven fractures in impermeable rocks. Int. J. GeoMech. 4 (1), 35–45. https://doi.org/10.1061/(ASCE)1532-3641(2004)4:1(35).
Fan, M.T., Li, J., Liu, G.H., 2019. Study on the sealing integrity of cement sheath during volume fracturing of shale gas of horizontal well. Cluster Comput. 22 (2), 5009–5016. https://doi.org/10.1007/s10586-018-2469-4.
Farris, T., Kokini, K., Demir, I., 1989. The cylindrical crack. J. Appl. Mech. 56, 981–983. https://doi.org/10.1115/1.3176203.
Feng, Y.C., Li, X., Grey, K.E., 2017. Development of a 3D numerical mode1 for quantifying fluid driven interface debonding of an injector well. Int. J. Greenh. Gas Control 62 (7), 76–90. https://doi.org/10.1016/j.ijggc.2017.04.008.
Garagash, D., 2000. Hydraulic fracture propagation in elastic rock with large toughness. The 4th North American Rock Mechanics Symposium, Seattle, 9058091554.
Garagash, D., Detournay, E., 2005. Plane-strain propagation of a fluid-driven fracture: small toughness solution. J. Appl. Mech. 72 (6), 916–928. https://doi.org/10.1115/1.2047596.
Gu, H., 1987. Study of Propagation of Hydraulically Induced Fractures. Ph.D. Dissertation. The University of Texas, Austin.
Gu, Y., Zhang, C., 2020. Novel special crack-tip elements for interface crack analysis by an efficient boundary element method. Eng. Fract. Mech. 239, 107302. https://doi.org/10.1016/j.engfracmech.2020.107302.
Hou, B., Chen, M., Zhang, B.W., Sang, Y., Cheng, W., Tan, P., 2015. Propagation of multiple hydraulic fractures in fractured shale reservoir. Chin. J. Geotech. Eng. 37 (6), 1041–1046. https://doi.org/10.11779/CJGE201506010 (in Chinese).
Huan, X., Xu, G., Zhang, Y., Sun, F., Xue, S., 2021. Study on thermo-hydro-mechanical coupling and the stability of a geothermal wellbore structure. Energies 14 (3), 649. https://doi.org/10.3390/en14030649.
Jacobs, T., 2019. To “right size” fractures, producers adopt robust monitoring and custom completions. J. Petrol. Technol. 71 (9), 38–46. https://doi.org/10.2118/0919-0038-JPT.
Jia, C.Z., 2017. Breakthrough and significance of unconventional oil and gas to classical petroleum geological theory. Petrol. Explor. Dev. 44 (1), 1–11. https://doi.org/10.1016/S1876-3804(17)30002-2.
Jiang, J.W., Li, J., Liu, G.H., Lian, W., Xi, Y., Yang, H.W., Li, W., 2020. Numerical simulation investigation on fracture debonding failure of cement plug/casing interface in abandoned wells. J. Petrol. Sci. Eng. 192 (3), 107226. https://doi.org/10.1016/j.petrol.2020.107226.
Kim, J.H., Paulino, G.H., 2007. On fracture criteria for mixed-mode crack propagation in functionally graded materials. Mech. Adv. Mater. Struct. 14 (4). https://doi.org/10.1080/15376490600790221, 227-224.
Kumar, D., Ghassemi, A., 2016. A three-dimensional analysis of simultaneous and sequential fracturing of horizontal wells. J. Petrol. Sci. Eng. 146, 1006–1025. https://doi.org/10.1016/j.petrol.2016.07.001.
Lecampion, B., Bunger, A., Kear, J., Quesada, D., 2013. Interface debonding driven by fluid injection in a cased and cemented wellbore. Modelling and experiments. Int. J. Greenh. Gas Control 18 (7), 208–223. https://doi.org/10.1016/j.ijggc.2013.07.012.
Lecampion, B., Quesada, D., Loizzo, M., Bunger, A., Kear, J., Deremble, L., Deroches, J., 2011. Interface debonding as a controlling mechanism for loss of well integrity: importance for CO_2 injector wells. Energy Proc. 4, 5219–5226. https://doi.org/10.1016/j.egypro.2011.02.500.
Li, Y., Chen, Y., Jin, J.Z., Jiang, L., Ding, F., Yuan, X., 2017a. Cement ring interface crack propagation under volume fracturing in shale gas well. Acta Pet. Sin. 38 (1), 105–111. https://doi.org/10.7623/syxb201701012 (in Chinese).
Li, Y.W., Jia, D., Rui, Z.H., Peng, J.Y., Fu, C.K., Zhang, J., 2017b. Evaluation method of rock brittleness based on statistical constitutive relations for rock damage. J. Petrol. Sci. Eng. 153, 123–132. https://doi.org/10.1016/j.petrol.2017.03.041.
Li, Y.W., Long, M., Tang, J.Z., Chen, M., Fu, X.F., 2020. A hydraulic fracture height mathematical model considering the influence of plastic region at fracture tip. Petrol. Explor. Dev. 47, 184–195. https://doi.org/10.1016/S1876-3804(20)60017-9.
Luo, A., Li, Y.M., Wu, L., Peng, Y., Tang, W., 2021. Fractured horizontal well productivity model for shale gas considering stress sensitivity, hydraulic fracture azimuth, and interference between fractures. Nat. Gas. Ind. B 8 (3), 278–286. https://doi.org/10.1016/j.ngib.2021.04.008.
Michael, A., 2021. Hydraulic fractures from non-uniform perforation cluster spacing in horizontal wells: laboratory testing on transparent gelatine. J. Nat. Gas Sci. Eng. 9, 104158. https://doi.org/10.1016/j.jngse.2021.104158.
Nagashima, T., Omoto, Y.H., Tani, S., 2003. Stress intensity factor analysis of interface cracks using X-FEM. Int. J. Numer. Methods Eng. 56 (8), 1151–1173. https://doi.org/10.1002/nme.604.
Olson, J.E., 2004. Predicting fracture swarms—the influence of subcritical crack growth and the crack-tip process zone on joint spacing in rock. Geological Society, London, Special Publications 231 (1), 73–88. https://doi.org/10.1144/GSL.SP.2004.231.01.05.
Olson, J.E., 2007. Fracture aperture, length and pattern geometry development under biaxial loading: a numerical study with applications to natural, cross-jointed systems. Geological Society London Special Publications 289 (1), 123–142. https://doi.org/10.1144/SP289.8.
Olson, J., Pollard, D.D., 1989. Inferring palaeostresses from natural fracture patterns: a new method. Geology 17 (4), 345–348. https://doi.org/10.1130/0091-7613(1989)017<0345:IPFNFP>2.3.CO;2.
Piva, A.A., 1982. A crack along a circular interface between dissimilar media. Meccanica 17 (2), 85–90. https://doi.org/10.1007/BF02135007.
Rice, J.R., 1988. Elastic fracture concepts for interfacial cracks. J. Appl. Mech. 55 (1), 98–103. https://doi.org/10.1115/1.3173668.
Saint-Marc, J., Garnier, A., Bois, A.P., 2008. Initial state of stress: the key to achieving long-term cement-sheath integrity. In: SPE Annual Technical Conference and Exhibition. https://doi.org/10.2118/116651-MS.
Sheikhmali, R., 2016. Numerical Simulation of Multiple Hydraulic Fractures Propagation Using XFEM-Based CZM to Determine the Proper Spacing of the Perforation Clusters. The University of Calgary, Canada.
Shi, Y.C., Li, B., Guo, B.Y., Guan, Z.C., Hui, L., 2015. An analytical solution to stress state of casing-cement sheath-formation system with the consideration of its initial loaded state and wellbore temperature variation. Int. J. Emerg. Technol.Adv. Eng 5 (1), 59–65.
Sneddon, I.N., Elliot, H.A., 1946. The opening of a Griffith crack under internal pressure. Q. Appl. Math. 4 (3), 262–267. https://doi.org/10.1090/qam/17161.
Sun, L.D., Liu, H., He, W.Y., Li, G.X., Zhang, S.C., Zhu, R.K., Jin, X., Meng, S.W., Jiang, H., 2021. An analysis of major scientific problems and research paths of Gulong shale oil in Daqing Oilfield, NE China. Petrol. Explor. Dev. 48 (3), 527–540. https://doi.org/10.1016/s1876-3804(21)60043-5.
Taleghani, A.D., 2011. Modeling simultaneous growth of multibranch hydraulic fractures. In: The 45th US Rock Mechanics/Geomechanics Symposium.
Tan, P., Jin, Y., Xiong, Z.Y., Chen, M., Hou, B., 2018. Effect of interface property on hydraulic fracture vertical propagation behaviour in layered formation based on discrete element modelling. J. Geophys. Eng. 15 (4), 1542–1550. https://doi.org/10.1088/1742-2140/aaa8ab.
Toya, M., 1974. A crack along the interface of a circular inclusion embedded in an infinite solid. J. Mech. Phys. Solid. 22 (5), 325–348. https://doi.org/10.1016/0022-5096(74)90002-7.
Wang, W., Taleghani, A.D., 2017. Impact of hydraulic fracturing on cement sheath integrity: a modelling approach. J. Nat. Gas Sci. Eng. 44, 265–277. https://doi.org/10.1016/j.jngse.2017.03.036.
Wang, Y.B., Liu, K., Gao, D., 2021. Investigation of the interface cracks on the cement sheath stress in shale gas wells during hydraulic fracturing. J. Petrol. Sci. Eng. 205 (4), 108981. https://doi.org/10.1016/j.petrol.2021.108981.
Wang, Y.H., 2016. Numerical investigation of fracture spacing and sequencing effects on multiple hydraulic fracture interference and coalescence in brittle and ductile reservoir rocks. Eng. Fract. Mech. 157, 107–124. https://doi.org/10.1016/j.engfracmech.2016.02.025.
Wu, K., 2014. Numerical Modelling of Complex Hydraulic Fracture Development in Unconventional Reservoirs. Ph.D. Dissertation. The University of Texas, Austin.
Wu, K., Olson, J.E., 2015. Simultaneous multifracture treatments: fully coupled fluid flow and fracture mechanics for horizontal wells. SPE J. 20 (2), 337–346. https://doi.org/10.2118/167626-PA.
Xu, B.X., Li, X.F., Shao, C., Chen, D., Huang, Y., Hu, X.D., 2011. Determination methods of well pattern and spacing for coalbed methane reservoir considering hydraulic fractures. Coal Geol. Explor. 39 (4), 16–19. https://doi.org/10.1007/s12182-011-0118-0 (in Chinese).
Xu, J., Fu, L., Mutoh, Y., 2000. Elastic-plastic boundary element analysis of interface edge in bonded dissimilar materials. J. Soc. Mater. Sci.Jpn. 49 (8), 857–861. https://doi.org/10.2472/jsms.49.857.
Xu, J.X., Yang, L.F., Liu, Z., Ding, Y.H., Gao, R., Wang, Z., Mo, S.Y., 2021. A new approach to embed complex fracture network in tight oil reservoir and well productivity analysis. Nat. Resour. Res. 30 (4), 2575–2586. https://doi.org/10.1007/s11053-021-09845-1.
Xu, J.X., Ding, Y.H., Yang, L.F., Wang, Z., Liu, Z., Gao, R., 2018a. Analysis of stress interference and geometry of hydraulic fractures based on the extended finite element method. Nat. Gas Geosci. 29 (9), 1356–1363. https://doi.org/10.11764/j.issn.1672-1926.2018.07.007 (in Chinese).
Xu, Y., Lei, Q., Chen, M., Wu, Q., Yang, N.Y., Weng, D.W., Li, Q.B., Jiang, H., 2018b. Progress and development of volume stimulation techniques. Petrol. Explor. Dev. 45 (5), 874–887. https://doi.org/10.1016/S1876-3804(18)30097-1.
Yan, Y., Guan, Z.C., Xu, S.Q., Wang, S.L., Song, S.W., 2020. Numerical simulation on microannulus propagation of cementing interface during hydraulic fracturing. J. Univ. Pet., China (Ed. Nat. Sci.) 45 (5), 932–947. https://doi.org/10.3969/j.issn.1673-5005.2020.03.007 (in Chinese).
Yang, S.C., Song, L., Li, Z., Huang, S.M., 2009. Experimental investigation on fracture toughness of interface crack for rock/concrete. Int. J. Mod. Phys. B 22 (31n32), 6141–6148. https://doi.org/10.1142/S0217979208051704.
Yin, F., Hou, D.L., Liu, W., Deng, Y. Novel assessment and countermeasure for microannulus initiation of cement sheath during injection/fracturing. Fuel. 252 (15): 157-163. https://doi.org/10.1016/j.fuel.2019.04.018..
Yong, L., Chen, Y., Jin, J.Z., Jang, L., Ding, F., Yuan, X., 2017. Cement ring interface crack propagation under volume fracturing in shale gas well. Acta Pet. Sin. 38 (1), 105–111. https://doi.org/10.7623/syxb20170101 (in Chinese).
Yuuki, R., Liu, J.Q., Xu, J.Q., Kim, Y.H., 1994. Study on the mixed mode fracture criterion of interface crack. Zairyo 43 (493), 1206–1210. https://doi.org/10.2472/jsms.43.1206.
Yuuki, R., Liu, J.Q., Xu, J.Q., Ohira, T., Ono, T., 1993. Fracture tests and evaluation of interface crack under mixed mode condition. Nihon Kikai Gakkai Ronbunshu, A Hen/Transactions of the Japan Society of Mechanical Engineers, Part A. 59 (557),

74–80. https://doi.org/10.1299/kikaia.59.74.
Zeng, Q.D., Yao, J., 2016. Numerical simulation of fracture network generation in naturally fractured reservoirs. J. Nat. Gas Sci. Eng. 30, 430–443. https://doi.org/10.1016/j.jngse.2016.02.047.
Zhang, J., Li, Y.W., Pan, Y.S., Wang, X.Y., Yan, M.S., Shi, X.D., Zhou, X.J., Li, H.L., 2021. Experiments and analysis on the influence of multiple closed cemented natural fractures on hydraulic fracture propagation in a tight sandstone reservoir. Eng. Geol. 281, 105981. https://doi.org/10.1016/j.enggeo.2020.105981.
Zhang, M., Bachu, S., 2011. Review of integrity of existing wells in relation to CO_2 geological storage: what do we know? Int. J. Greenh. Gas Control 5 (4), 826–840. https://doi.org/10.1016/j.ijggc.2010.11.006.
Zhong, H., Ooi, E.T., Song, C.M., Ding, T., Lin, G., Li, H.J., 2014. Experimental and numerical study of the dependency of interface fracture in concrete–rock specimens on mode mixity. Eng. Fract. Mech. 124–125, 287–309. https://doi.org/10.1016/j.engfracmech.2014.04.030.
Zhu, H.Y., Deng, J.G., Li, S.Y., Chen, Z.J., Yan, W., Hu, L.B., Lin, H., Yan, C.L., 2013. Numerical simulation and laboratory experiments of hydraulic fracturing of highly deviated well. Appl. Mech. Mater. 275–277, 278–281. https://doi.org/10.4028/www.scientific.Net/AMM.275-277.278.